
Book Section:
Andreev, Andrey orcid.org/0000-0003-2828-0262 and Van Duppen, Piet (2018) Alpha Decay and Beta-Delayed Fission: Tools for Nuclear Physics Studies. In: Scheidenberger, Christopher and Pfutzner, Marek, (eds.) The Euroschool on Exotic Beams. Lecture Notes in Physics, LPN, vol. 948. Springer, pp. 65-116.

https://doi.org/10.1007/978-3-319-74878-8_3

Noname manuscript No.
(will be inserted by the editor)

Alpha decay and beta-delayed fission: tools for nuclear-physics studies

P. Van Duppen, A.N. Andreyev

Received: date / Accepted: date

Contents

1 Introduction and physics motivation . . . 2
2 Alpha decay . . . 3
2.1 Basics of the α-decay process . . . 3
2.2 Theoretical approaches to the α-decay process . . . 7
2.2.1 Semi-classical approach . . . 7
2.2.2 Microscopic description . . . 12
2.3 Experimental approaches and observables . . . 12
2.4 Examples of nuclear-structure information extracted from α-decay studies . . . 16
2.4.1 Super-allowed α decay around ^{100}Sn . . . 16
2.4.2 Shape coexistence in the neutron-deficient lead region . . . 18
2.4.3 Searching for the heaviest elements . . . 20
3 Beta-delayed fission . . . 22
3.1 Introduction to low-energy fission . . . 22
3.2 Mechanism of beta-delayed fission, conditions to occur, observables . . . 25
3.3 Production of βDF nuclei and determination of their properties . . . 29
3.4 Recent βDF results at recoil separators . . . 30
3.5 A new approach to study βDF at the ISOLDE mass separator at CERN . . . 32
3.5.1 New island of asymmetric fission in the neutron-deficient mercury region: the case of ^{180}Tl . . . 34
3.5.2 Mass-asymmetry in ^{180}Tl and in ^{238}U - what is the difference? . . . 34
3.5.3 Multimodal fission in the transitional neutron-deficient region above Z=82 . . . 37
3.5.4 Complementary approaches to study low-energy fission in the lead region . . . 41
3.6 β-delayed fission rates and their use to determine fission barrier heights . . . 42

P. Van Duppen
Insituut voor Kern- en Stralingsfysica
Departement of Physics and Astronomy
KU Leuven, Belgium
E-mail: Piet.VanDuppen@kuleuven.be

A.N. Andreyev
Department of Physics
University of York, U.K.
E-mail: Andrei.Andreyev@york.ac.uk

4 Conclusion and outlook 45

Abstract α decay and β-delayed fission are two important decay modes of heavy exotic nuclei. Experimental α and β-delayed fission studies deliver significant nuclear-structure information in regions of the nuclear chart with limited accessibility. This information is important to improve the predictability of contemporary nuclear models used for e.g. nuclear astrophysics calculations. The basic principles and the current understanding of α and β-delayed fission decay are introduced. Examples of recent experiments and their impact on the understanding of heavy nuclei are presented.

Keywords α decay · β-delayed fission · radioactive ion beams

PACS 20 · 23 · 23.60.+e · 25.85.-w · 29.38.-c ·

1 Introduction and physics motivation

As emphasized in the previous volumes of The Euroschool on Exotic Beams Lecture Notes (volume I - IV), nuclides with a proton-to-neutron ratio different from stable nuclei are ideal laboratories to study the strong and weak interaction acting in the nuclear medium (see e.g. [1]). Combining experimental and theoretical work improves our understanding and, in particular, increases the predictive power of nuclear models. The latter is essential as, in spite of the tremendous progress in radioactive ion beam research, certain regions of the nuclear chart, e.g. heavy nuclei close to the neutron drip line or the region of the superheavy elements, still remain poorly accessible for experimental studies. Understanding the nuclear properties is not only essential for nuclear physics but also for nuclear astrophysics and for applications.

Exotic nuclei can be investigated with several different methods like e.g. decay and in-beam studies, mass and laser spectroscopy, Coulomb excitation and nuclear reactions.

In the present Lecture Notes, we will discuss two radioactive decay modes: α decay and β-delayed fission (βDF). α decay, known since the beginning of the 20th century, was one of the first 'nuclear' decay modes to be discovered. Fission was discovered in 1938. Interestingly, soon after the respective discoveries, a sufficiently detailed qualitative understanding of the decay mechanism was realized - α decay in 1928 [2–4] and fission literary a few months after its discovery [5,6].

α decay and βDF happen in heavy nuclei, have quantum-mechanical tunneling through a potential barrier in common and are pivotal for nuclear-physics research and other related fields. For example, in nuclear astrophysics studies, α-capture reactions (equivalent to the inverse α-decay process) are important for nucleosynthesis and βDF, together with other fission modes, determine the so-called "fission recycling" in the r-process nucleosynthesis (see e.g. [7,8]).

These notes report on the current understanding of α and βDF decay and discuss recent examples of experimental studies and their impact on nuclear

structure. They are not aimed to give a concise review of the theory of these processes, but rather to supply the essential elements necessary to understand the way nuclear-structure information is deduced from these experiments.

A general introduction on α decay starting from the well-known Geiger-Nuttall (GN) rule and its modern versions followed by a global discussion on semi-classical and microscopic approaches are presented. New insights in the success of the GN rule have surfaced recently and will be discussed along with selected examples where α decay played a key role.

βDF is a sub-class of beta-delayed particle emission processes. It is an exotic process coupling beta decay and fission. A special feature of βDF is that it can provide low-energy fission data (excitation energy of the fissioning nucleus < 10 MeV) for very neutron-deficient and neutron-rich nuclei which do not fission spontaneously and which are difficult to access by other methods. Some of these nuclei have recently become reachable for experiments due to new development in production techniques of radioactive beams [9], especially in the lead region. Already these first exploratory experiments led to surprising discoveries which will be highlighted in these lecture notes.

This chapter is structured in the following way. Sec. 2.1 discusses the basics of the α-decay process while Sec. 2.2 presents its current understanding from a semi-classical and a microscopic viewpoint. The experimental methods are summarized in Sec. 2.3 and recent examples of α-decay studies are given in Sec. 2.4. Sec. 3.1 gives an introduction in low-energy fission while the mechanism of βDF is discussed in Sec. 3.2. An overview of the production methods of βDF nuclei is presented in Sec. 3.3 and Sec. 3.4 and 3.5 discuss recent results obtained at radioactive beam facilities. A discussion on the βDF rates and their use to investigate the fission barrier height is presented in Sec. 3.6. A summary and conclusion are given in Sec. 4.

2 Alpha decay

2.1 Basics of the α-decay process

In this section, the basics of the α-decay process will be shortly reviewed. More detailed descriptions and discussions are available from a number of excellent nuclear-physics and nuclear-chemistry textbooks (see e.g. [10–12]), review papers [13] and in the previous volumes of these lecture notes series [14,15].

Every radioactive decay process is characterized by its energy balance and its transition probability. The α decay of the parent nucleus ($^{A}_{Z}X_{N}$) to the daughter nucleus $^{A-4}_{Z-2}Y_{N-2}$ can be represented by:

$$^{A}_{Z}X_{N} \rightarrow ^{A-4}_{Z-2}Y_{N-2} + ^{4}_{2}He_{2} + Q_{\alpha} \quad (1)$$

where A, Z and N are, respectively, the atomic mass number, proton number and neutron number of the α-decaying nucleus. The Q_{α} value represents the negative of the α-particle binding energy of the parent nucleus and can be

obtained from mass differences or differences in binding energy of the parent nucleus and the sum of the daughter nucleus and the α particle:

$$Q_\alpha = (M({}^{A}_{Z}X_N) - (M({}^{A-4}_{Z-2}Y_{N-2}) + M_\alpha))c^2 \tag{2}$$

$$Q_\alpha = (BE(A-4, Z-2) + 28.3\ MeV) - BE(A, Z) \tag{3}$$

where M represents the mass and BE the total binding energy expressed in MeV. As the differences in electron binding energies between parent and daughter are small, the nuclear masses can be replaced by atomic masses which are tabulated in the Atomic Mass Evaluation (AME) tables [16]. When the α-binding energy becomes negative, resulting in a positive Q_α value, the nucleus can undergo spontaneous α decay. As shown in e.g. Fig. 4.2 from [10], along the chart of nuclides this happens for nuclei with mass atomic number $A\geq$ 150. However, because of the strong (exponential) dependence of the α-decay probability on the Q_α-value, α decay only becomes the dominant decay mode for some of the more heavy nuclei. Interesting to note is that even the doubly magic ^{208}Pb nucleus is unstable with respect to α decay with a $Q_\alpha = 517.2(1.3)$ keV [17]. Based on the Geiger-Nuttall rule (see further) this would lead to a partial α-decay half life of $\sim 10^{123}$ years, much beyond the age of the Universe which justifies the notation that ^{208}Pb is a stable nucleus. The longest half-life measured for an α-emitting nucleus has been obtained for ^{209}Bi where, using bolometric techniques, a half life of $1.9(2) \times 10^{19}$ years and an α-decay energy of 3.137 MeV were measured [18].

α decay is a two-body process and the kinetic energy released is shared between the α particle and the recoiling nucleus following conservation of energy and momentum. The relation between Q_α and the kinetic energy of the α particle (E_α) is given as:

$$Q_\alpha = E_\alpha \left(\frac{M_d + M_\alpha}{M_d}\right) \tag{4}$$

$$\sim E_\alpha \left(\frac{A}{A-4}\right) \tag{5}$$

where M_p and M_d are the mass of the parent and daughter nuclei, respectively. After α decay, the typical recoil energy is about 100 keV for an $A = 200$ parent nucleus and a Q_α value of 5 MeV. The influence of the recoil effect has to be considered carefully in experiments with e.g. thin α sources as part of the daughter nuclei recoils out of the source sample risking to influence the measurements (see section 2.3).

From the half life of the nucleus ($T_{1/2}$) and the α-decay branching ratio (b_α), the partial α-decay half life ($T_{1/2,\alpha}$) or mean lifetime (τ_α), decay constant (λ_α) and decay width (Γ_α) can be deduced:

$$T_{1/2,\alpha} = \left(\frac{T_{1/2}}{b_\alpha}\right) = \tau_\alpha\ ln2 \tag{6}$$

$$\tau_\alpha \Gamma_\alpha = \frac{\Gamma_\alpha}{\lambda_\alpha} = \hbar \tag{7}$$

A connection between the α-decay energy and the partial α-decay half-life was first established by Geiger and Nuttall who discovered a linear relationship between the logarithm of the α-decay constant and the logarithm of the range of α particles in matter [19,20]. This led to the well known Geiger-Nuttall (GN) rule for α decay which, in its simplified form, can be written as:

$$Log T_{1/2,\alpha} = \frac{A}{\sqrt{Q_\alpha}} + B \tag{8}$$

where A and B are constants, deduced from a fit to the experimental data. The first successful theoretical explanation of this dependence was given by Gamow [2] and independently by Condon and Gurney [3,4], who explained α decay as the penetration (tunneling) through the Coulomb barrier. This was the first application of quantum mechanics to a nuclear-physics problem. This so-called semi-classical description of the α-decay process assumes that the α particle is 'pre-formed' inside the nucleus with a certain probability and it 'collides' with the Coulomb barrier. Upon every collision, it has a finite probability to tunnel through the barrier ([10–12]). Fig. 1 gives a schematic representation. The α particle moves in an attractive, effective potential created by the strong interaction (V_N) and the Coulomb interaction (V_C) and is quasi-bound by the Coulomb barrier (details are given in Sec. 2.2). The square well potential (V_N) and the Coulomb interaction as deduced from a spherical charge distribution are approximations; however, they give a reasonable description of the basic features of the α-decay process.

As α decay involves quantum mechanical tunneling through the Coulomb barrier, its partial half life or transition probability depends exponentially on the Q_α value as represented by the GN rule. Figure 2 shows the logarithm of the experimental partial α-decay half lives (in s) for the even-even Yb-Ra nuclei with neutron number $N< 126$ as a function of $Q_\alpha^{-1/2}$ (in $\mathrm{MeV}^{-1/2}$). For most of the isotopic chains considered, the GN rule gives a reliable description except when crossing the magic N=126 shell and, as will be discussed later, for the case of the polonium (Z=84) isotopic chain. Note that the A and B parameters are dependent on Z and experimental data suggest a linear dependence on Z as shown in Fig. 3. This was already introduced as a generalization of the GN rule by Viola and Seaborg [21]. Recent studies, which investigate the Geiger-Nuttall rule from a microscopic perspective, give rise to different parameterizations or dissimilar Z-dependencies of the A and B parameters. However, as will be discussed further, the basic linear $\log(T_{1/2})$ versus $Q_\alpha^{-1/2}$ dependence, deduced from systematic studies remains (see e.g. [22–24]).

Next to the ground-state to ground-state α decay also decay to excited states can happen, giving rise to what is referred to as fine structure in the α-decay energy spectra. Studying the fine structure in the α decay reveals the energy of excited states, while from the relative intensities for different fine structure decay branches information on the structure of different states can

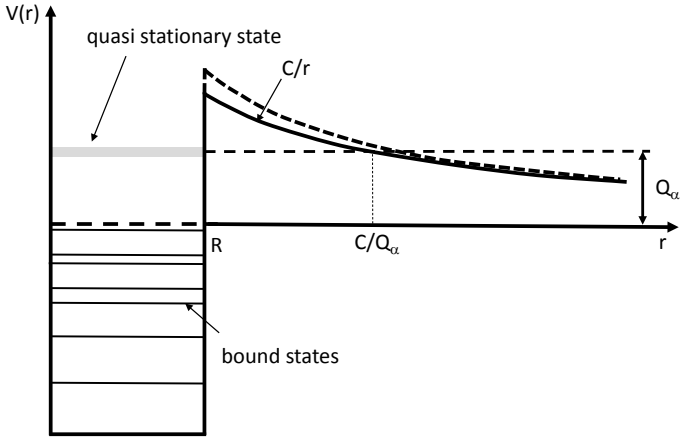

Fig. 1 A one-dimensional representation of the α-decay process. The full line shows the nuclear square well and Coulomb potential (see equation 10, 11). R is the nuclear radius and $C=\frac{2(Z-2)e^2}{4\pi\epsilon_0}$ represents the constant due to the Coulomb interaction with ϵ_0 the vacuum permittivity. The dashed line shows the sum of the Coulomb potential and the centrigual part of the potential ($C/r + l_\alpha(l_\alpha+1)\hbar^2/2\mu r^2$) with l_α representing the transferred angular momentum in the α-decay process and μ the reduced mass of the α particle and daughter nucleus.

be obtained (see e.g. Sec. 2.4). As angular momentum needs to be conserved, the α particle might have to carry angular momentum depending of the spin difference between the parent and the daughter states. As in the ^{4}He nucleus the protons and neutrons are coupled to spin and parity $I^\pi = 0^+$, the angular momentum carried away by the α particle is solely of orbital character which introduces a parity selection rule. If the α particle's orbital angular momentum is represented by l_α, the parity change associated with the α decay should then be $(-1)^{l_\alpha}$. For example, the α decay from the 0^+ ground state of an even-even nucleus towards an excited 2^+ state requires the α particle to take away two units of angular momentum and is allowed, however the decay towards a 1^+ state is forbidden.

α decay involving non-zero orbital angular momentum gives rise to an effective potential barrier consisting of a Coulomb and a centrifugal part that is proportional to $l_\alpha(l_\alpha + 1)\hbar^2/2\mu r^2$. This modified potential, shown in Fig. 1, becomes higher and the barrier thicker, which in turn decreases the α-decay probability. As will be shown in sec. 2.4, the study of the fine structure in e.g. the neutron-deficient lead region has allowed to identify low-lying 0^+ states and supported the appearance of shape coexistence at very low excitation energy.

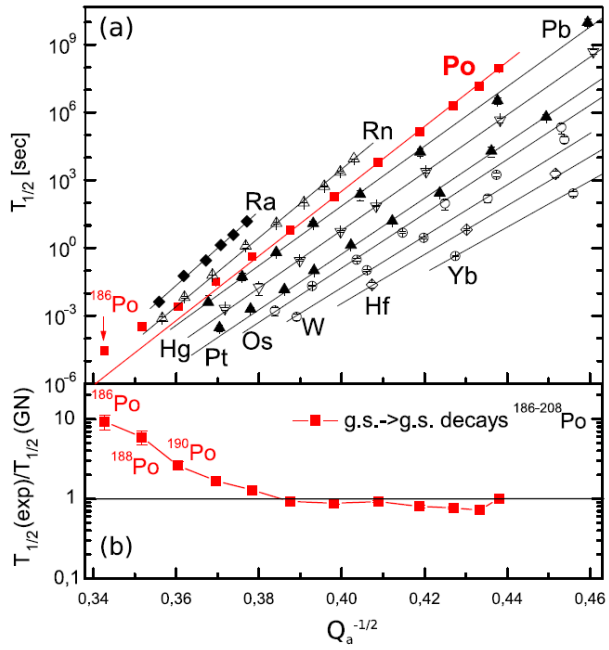

Fig. 2 (a) Geiger-Nuttall plot for selected isotopic chains. The straight lines show the description of the GN rule from which the $A(Z)$ and $B(Z)$ values are fitted for each isotopic chain. The results are presented in Fig. 3. (b) The deviation of the experimental α-decay half-lives from those predicted by the GN rule for the light Po isotopes. Adapted from [25].

2.2 Theoretical approaches to the α-decay process

2.2.1 Semi-classical approach

In this section we will discuss the semi-classical description of the α-decay process. Following the approach similar to [26], the parameters of the GN rule will be extracted and, more generally, an expression will be deduced to evaluate the α-formation probability from experimental data.

The α-decay constant can be written as:

$$\lambda_\alpha = p_\alpha \nu T \tag{9}$$

where p_α represents the probability to form an α particle inside the nucleus, ν the collision frequency of the α particle's assault against the barrier and T the tunneling probability through the barrier. The one-dimensional potential, as shown in Fig. 1, gives all the ingredients necessary to discuss the α-decay process.

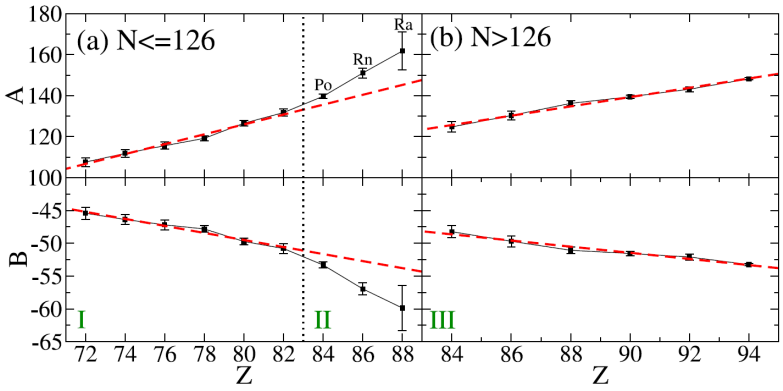

Fig. 3 (a) The coefficients $A(Z)$ and $B(Z)$ for even-even nuclei with $Z \leq 82$ (I) and, $Z > 82$ and $N \leq 126$ (II). (b) Same as (a) but for nuclei with $Z > 82$ and $N > 126$ (III). The red dashed lines are linear fits through the data of region I (a) and III (b). Adapted from [25]

The tunneling probability can be calculated using different levels of complexity in the assumed potentials (see for example [10,11] and for a recent review see [24]). Following [26] and neglecting the centrifugal barrier, thus only considering l_α=0, the potential can be written as

$$V(r) = -V_N + C/R \;\; (r < R) \tag{10}$$

$$V = \frac{C}{r} \;\; (r > R) \tag{11}$$

$$C = \frac{2(Z-2)e^2}{4\pi\epsilon_0} \tag{12}$$

where Z is the parent's proton number, e is the electron charge (in Coulomb), ϵ_0 the vacuum permittivity and R the radius of the daughter nucleus (see Fig. 1). The potential in the nuclear interior ($r < R$) is dominated by the nuclear part, while outside the Coulomb part takes over. Note that at this stage a constant Coulomb potential was assumed inside the nucleus which is an over simplification. One can then calculate the α-decay width using the Wentzel-Kramers-Brillouin (WKB) approach as:

$$\Gamma_\alpha = \left(\frac{p_\alpha \hbar^2 K}{2\mu R}\right) exp\left(-2\int_R^{C/Q_\alpha} k(r)dr\right) \tag{13}$$

where μ represents the reduced mass of the α particle and daughter nucleus, while K and k(r) are the wave numbers in the internal ($r < R$) and barrier regions ($R < r < C/Q_\alpha$), respectively,

$$K = \left(\frac{2\mu}{\hbar^2}\left(Q_\alpha + V_N - \frac{C}{R}\right)\right)^{1/2} \tag{14}$$

$$k(r) = \left(\frac{2\mu}{\hbar^2}\left(\frac{C}{r} - Q_\alpha\right)\right)^{1/2} \tag{15}$$

leading finally to an expression of the partial α-decay half life,

$$T_{1/2,\alpha} = \frac{2ln2}{p_\alpha}\left(\frac{\mu R}{\hbar K}\right) exp\left(2\int_R^{C/Q_\alpha} k(r)dr\right) \tag{16}$$

One recognizes the α-particle formation probability (p_α), a measure for the collision time (the term between the first brackets) and the tunneling probability as represented by the exponential function of the integral. Buck et al. were able to describe experimental α-decay half lives by adjusting the inner radius (R) on the Q_α value using the Bohr-Sommerfeld quantization condition:

$$R = \frac{\pi}{2}\frac{G+1}{K} \tag{17}$$

Here, the 'global' quantum number G equals $2n+l_\alpha$, with n is the harmonic oscillator quantum number and l_α the angular momentum transfer. This description assumes that the α particle is constructed from the valence protons and neutrons in the heavy nucleus (see Sec. 2.2.2). The value of G was also adapted to achieve the best agreement between theory and experiment. For example, from a simple perspective, the α decay of ^{212}Po to ^{208}Pb involves the clustering of two protons above the Z=82 (n_π=5) and two neutrons above the N=126 (n_ν=6) shell, which, for $n = n_\nu + n_\pi$, results in values of G around 22 [26]. By adjusting V_N to 140 MeV and assuming p_α=1, a good overall agreement between experimental and calculated values was obtained provided G was changed from 22 to 24 for nuclei with $N \leq 126$ and $N > 126$, respectively [26,27]. The influence of more 'realistic' barriers, including a centrifugal barriers, was also evaluated [28]. The success of these and other cluster-based calculations supports the assumption of α-cluster formation inside nuclei.

Before turning to a more microscopically-based description of the formation amplitude, let us evaluate the tunneling through the barrier by calculating the integral in (16). This leads to the the following general relation [10,11],

$$LogT_{1/2,\alpha} = aZ\sqrt{\frac{\mu}{Q_\alpha}} + b\sqrt{\mu Z} + c \tag{18}$$

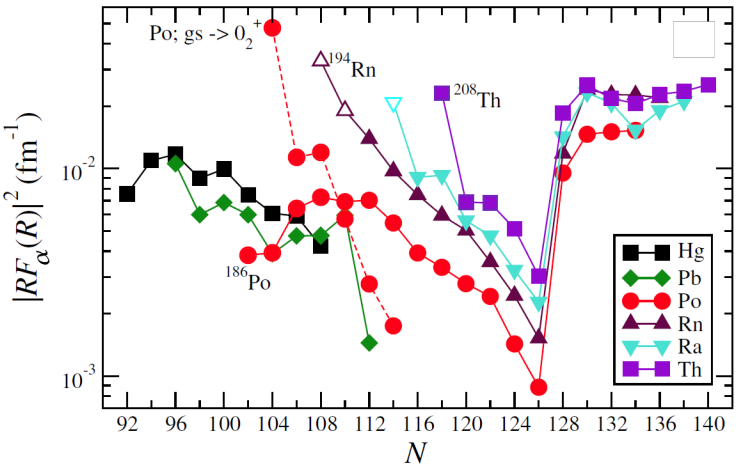

Fig. 4 α-particle formation probability for the decays of even-even isotopes in the mercury to thorium region as a function of neutron number of the parent nucleus. The values were obtained using equation (20) combined with experimental Q_α and $T_{1/2,\alpha}$ values. The symbols connected by a dashed line show the $|RF_\alpha(R)|^2$ values for fine structure α decays of polonium isotopes to the 0_2^+ states in the corresponding lead daughter nuclides. Adapted from [29].

This expression resembles very much the Geiger-Nuttall rule (8), however, the linear dependence of the coefficients on Z, as extracted from the experimental data [21,25], is not observed.

Rasmussen introduced a reduced α-decay width deduced from a combination of the experimental α-decay constant and a calculated tunneling probability [30]. This gave rise to:

$$\lambda_\alpha = \delta^2 \frac{T}{h} \tag{19}$$

The reduced α-decay width, δ^2, is expressed in keV, and is used in many papers to calculate hindrance factors in the fine structure α-decay studies.

Recently, a general description of α and cluster decay using the R-matrix approach was proposed [31,32]. From R-matrix theory, one obtains the following expression for the decay half life,

$$T_{1/2,\alpha} \simeq \frac{ln2}{v} \left| \frac{H}{RF_\alpha(R)} \right|^2 \tag{20}$$

with H the Coulomb-Hankel function [33], v the outgoing velocity of the α particle and $|RF_\alpha(R)|^2$ the α-formation probability at radius R. Note that the

velocity is equivalent to $\hbar K/\mu$ in (16). Qi et al. realized that the the Coulomb-Hankel function, that describes the tunneling process, can be approximated by an analytical expression and they obtained the following global expression for the α- decay half life,

$$LogT_{1/2,\alpha} = a2Z\sqrt{\frac{\mathcal{A}}{Q_\alpha}} + b\sqrt{2Z\mathcal{A}(A_d^{1/3} + 4^{1/3})} + c \qquad (21)$$

with A_d the atomic mass number of the daughter nucleus and $\mathcal{A}$=$4A_d/(A_d+4)$ proportional to the reduced mass. Values for the constants a, b and c are reported [31,32], but important to note is that a and b are of similar magnitude, that a is positive, and b and c are negative with a value of c=-21.95. Again the GN rule dependence on Q_α is reproduced; however, a similar $\sqrt{Z}$ dependence of the second term as in (18) is observed. Expression (20) allows to extract the experimental formation probability using the experimental Q_α values and $T_{1/2,\alpha}$ values. This gives a more precise and unambiguous assessment of the clustering process compared to the reduced α-decay width from [30]. Fig. 4 shows the formation probability for the even-even nuclei from mercury to thorium. A behavior similar to the reduced α-width plots (see e.g. Fig. 3 from [34]) is observed. In [25] it was discussed that the GN rule is broken as soon as the $\log|RF_\alpha(R)|^2$ dependence on neutron number is not linear. Therefore a separate GN fit for $N > 126$ and $N < 126$ is performed (see Fig. 3).

It was furthermore underlined that the previously noticed success of the GN rule to describe the available data was somehow due to the limited data range within one isotopic series. A notorious exception are the polonium isotopes where a deviation from the GN rule up to a factor of ten has been reported for the most neutron deficient ^{186}Po decay (see Fig. 2). Because of the large data range - from ^{218}Po ($N = 134$) to ^{186}Po ($N = 102$) - deviations from the linear behavior in the formation probability could be observed. In addition, as will be discussed later, the fine structure in the α decay and nuclear-structure effects reveal an even larger discrepancy.

Finally, the linear Z-dependence of the $A(Z)$ and $B(Z)$ parameters in the GN rule deserves some further attention. It can be easily shown that this leads to a critical Q_α value where the α-decay half lives are equal irrespective of Z: all lines from the GN rule converge to the same point as can be seen by extrapolating the linear fit curves in Fig. 2. Using the coefficients reported in [25], for the isotopes with N<126, this corresponds to Q_α=20.2 MeV and $\log T_{1/2,\alpha}$ =-21.5. This is an un-physical effect and reinforces the limited validity range of the GN rule or other adaptations. Interesting to note, however, is that the critical $\log T_{1/2,\alpha}$ value is close to the typical semi-classical collision time of -21.1 (see [11]). By invoking similar conditions using the Universal Decay Law approach [31,32] gives a value of -21.95. A closer look to the expressions from [26] (see Eq. 16) and of the Universal Decay Law [31,32] (see Eq. 21) reveals that this condition corresponds to $Q_\alpha \simeq (2Z_d)/(A_d^{1/3}+4^{1/3})$ for the former and R=C/Q_α for the latter. These are Q_α values corresponding to the top of the one-dimensional Coulomb barrier.

2.2.2 Microscopic description

Determining the formation probability of an α particle inside a heavy nucleus from basic principles is challenging. Several microscopic calculations using shell model and cluster formation approaches, based on the early work by Mang, Fliessbach and Rasmussen [35,36], have been undertaken. In these calculations the α-particle formation probability at the surface of the daughter nucleus is calculated starting from the single-particle shell-model wave functions. Shell-model calculations applied for nuclei around the doubly magic ^{208}Pb nucleus reveal that the calculated α decay width underestimates the experimental value at least by one order of magnitude [36]. Further improvements complementing shell-model with cluster-model approaches in the framework of R-matrix calculations [37] to determine the cluster formation probability, lead to consistency between the calculated and the experimental α-decay width of ^{212}Po [38,33]. Following the description of [38,33,39], the key ingredient is a careful evaluation of the formation amplitude that represents an overlap integral of the parent α-decaying state with the daughter nucleus coupled to an α particle [39,25]. Several methods have been developed and applied to describe the α-decay process from a microscopic view point, including deformed nuclei [40], but a detailed review of such efforts is outside the scope of the present lecture notes and we refer the reader to [33,41,24]. One general conclusion from these works is that they support the large degree of clusterisation happening inside the nucleus which explains the success of the semi-classical approaches where cluster formation is implicitly assumed.

A lot of the work has been concentrated on the α decay of ^{212}Po to the doubly magic nucleus ^{208}Pb [38,33] which is considered as a text-book example of the fastest α decay observed. Recently, however, the super-allowed character of the α decay of ^{104}Te has been investigated theoretically [42]. This work was triggered by the experimental data obtained in the ^{109}Xe-^{105}Te-^{101}Sn α-decay chain [43,44] (see Sec. 2.4) and the importance of these studies was also emphasized in [14]. As the protons and neutrons that form the α particle are occupying similar single-particle orbitals for the $N = Z$ nuclei (around ^{100}Sn) but different ones for ^{212}Po, an increase in proton-neutron correlation and cluster formation probability is expected. The calculations reported in [42] support this interpretation.

In closing this part of the notes, we mention that several attempts have been undertaken to develop a common description of α decay, cluster decay (whereby the parent nucleus emits a heavier nucleus like e.g. ^{14}C) and fission. The reader is referred to [45,46] and references therein.

2.3 Experimental approaches and observables

The α-decaying medium heavy and heavy isotopes are typically produced using heavy-ion fusion evaporation reactions using beam energies around and above the Coulomb barrier, or high-energy proton induced spallation reac-

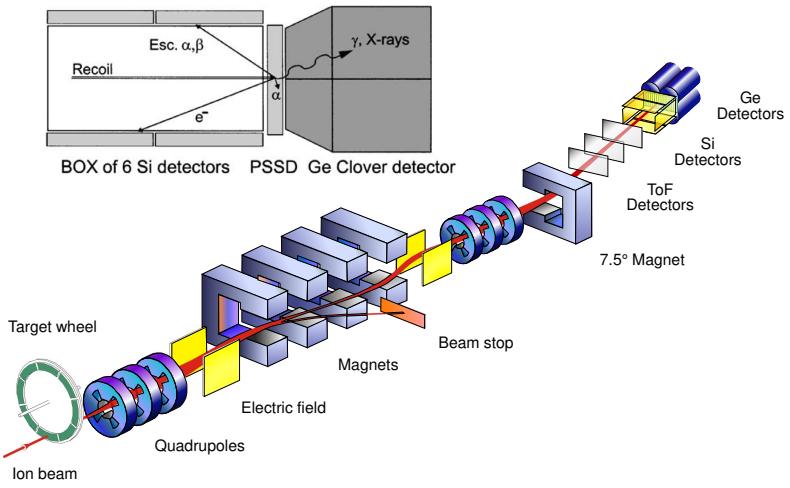

Fig. 5 Schematic layout of the SHIP velocity filter at GSI. The heavy ion beam enters SHIP from the left, hits the targets mounted on a rotating wheel. The recoil products, leaving the target with a rather broad angular distribution, are focused by the first triplet of quadrupole lenses. The sequence of perpendicular electric and magnetic fields, serving as a Wien filter, separates the recoils from the projectiles. Because of the large velocity difference between recoil products and the primary heavy ion beam, the latter is deviated from the former and stopped in the beam stop. The recoils are further focused by the second triplet of quadrupole lenses and finally implanted in the PSSD at the focal plane of SHIP. The inset shows the silicon box and germanium detection system surrounding the PSSD, and as well as typical decay channels (see text for details). Adapted from [53,54]

tions. In order to purify the reaction products from the primary and possibly other secondary beams, two complementary approaches are used: the 'in-flight' separation technique and the 'Isotope Separator On Line (ISOL)' technique. Heavy-ion beams are used for the former as 'in-flight' separation makes use of the reaction kinematics, while high-energy protons impinging on thick actinide targets (^{238}U or ^{232}Th) are used for the latter. α-decay studies have been performed at several different in-flight separators like SHIP and TASCA at GSI (Germany), RITU and MARA at JYFL (Finland), FMA and AGFA at Argonne, BGS ar Berkeley (USA), GARIS/GARIS2 at RIKEN (Japan), VASSILISSA/SHELS and DGFS at Dubna (Russia) (for a review on these facilities, see [47]). The two main ISOL-based facilities where α-decay studies are performed are ISOLDE [48] and TRIUMF [49]. For completeness, we note interesting results on the production and decay properties of suburanium isotopes following projectile fragmentation of ^{238}U at 1 GeV/u beams [50, 51]. Details on the ISOL and fragmentation approach have been described in previous chapters of these lecture notes series [52,9].

In Sec. 3.5, an experimental set-up used at ISOLDE-CERN for α and beta-delayed fission studies will be presented. In this section, dedicated to α decay, we will demonstrate the use of the method of α-α correlations which is extensively applied in modern experiments to study α decay and e.g. to synthesize new isotopes and elements. As an example, we discuss the α-decay study performed at the SHIP velocity filter at GSI to identify the new isotope ^{194}Rn [55]. The SHIP velocity filter [56,53,57] is shown schematically in Fig. 5. The nuclei of interest were produced in the heavy-ion fusion-evaporation reaction ^{52}Cr+^{144}Sm $\rightarrow$ ^{194}Rn+2n (evaporation of two neutrons) at several beam energies between 231 and 252 MeV and a typical intensity of 500-700 pnA. Eight enriched ^{144}Sm targets of 400 μg/cm^2 thickness were mounted on a rotating target wheel. The target rotation allows to spread the incoming beam over a larger target area to reduce the target temperature. This is especially necessary when using high beam intensities of heavy ions to reach e.g. the super heavy elements (see further). SHIP acts as a velocity filter using electrical and magnetic fields in a perpendicular configuration like a Wien filter. Due to the difference in kinematical properties of the primary beam, passing through the thin target, and of the nuclei of interest, recoiling from the target, they can be spatially separated by the filter. The primary beam is dumped in the beam dump, while the recoiling nuclei are implanted in a 300 μm thick 35×80 mm^2 16-strip position-sensitive silicon detector (PSSD) at the focal plane of SHIP. This detector measures the energy, time and position of recoils and their subsequent decays, e.g. α, fission and conversion electrons. Upstream of the PSSD, six silicon detectors of similar shape were mounted in a box geometry, see Fig. 5. The box detector can be used to reconstruct the energy of α particles and conversion electrons that escape from the PSSD in the backward hemisphere [54]. This increases the total detection efficiency for decays, up to ∼80%. Due to the position resolution of ∼0.5 mm along the strips, the whole PSSD can be considered as an array of 35 mm/0.5 mm ×16 strips ∼1100 effective detector pixels, which allows to reduce the rate of random correlations. As the identification is based on correlating the recoil implantation with subsequent decays (α, fission or electrons), this high degree of pixelation allows to extend the correlation times and thus the accessible range of half-lives. Nowadays, most advanced focal plane implantation detectors are double-sided strip detectors (DSSD), which have up to 120 strips × 60 strips = 7200 effective pixels. Combined with digital electronics read-out this results in a further performance increase.

The time and position correlations between the recoil implantation and the subsequent decays makes the identification of the isotopes unambiguous. For example, as shown in Fig. 6, by searching for four-fold recoil-α_1-α_2-α_3 events, observed within the same position of the PSSD, allowed to identify the new isotope ^{194}Rn. The identification of unknown α decays of ^{194}Rn was performed via establishing their time and position correlations with the *known* α decays of the daughter ^{190}Po ($T_{1/2}$=2.5 ms) and granddaughter ^{186}Pb ($T_{1/2}$ = 4.8 s).

The α-decay spectrum observed with a time condition between the arrival time of the recoil and the observation of the first α particle (ΔT(recoil-α_1) < 5

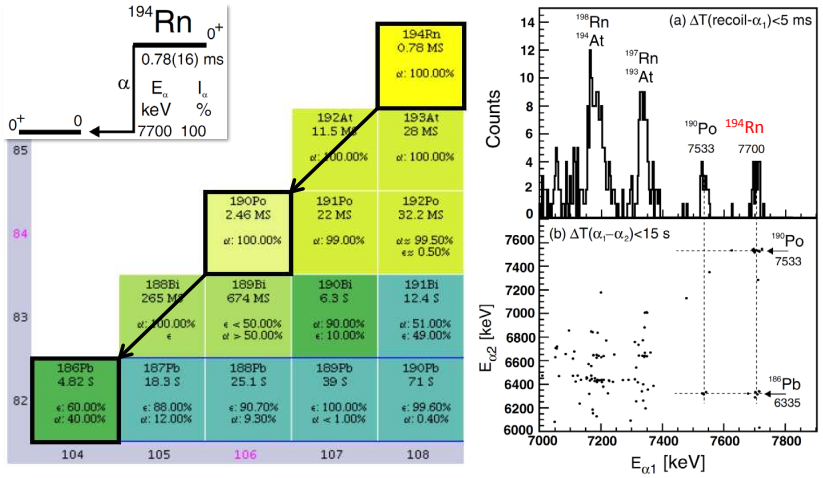

Fig. 6 Principles of identification of the new isotope ^{194}Rn in the reaction ^{52}Cr+^{144}Sm $\rightarrow$ ^{194}Rn+2n. (Left panel) The decay scheme of ^{194}Rn with the decay information and the triple α-decay sequence ^{194}Rn $\rightarrow$ ^{190}Po $\rightarrow$ ^{186}Pb$\rightarrow$ ^{182}Hg, used for identification. (Right panel - top) The α_1 decay spectrum obtained with a constraint on the time between the implantation of the recoiling nucleus and the subsequent first α decay. (Right panel - bottom) A two-dimensional correlation $E_{\alpha 1}$ versus $E_{\alpha 2}$ plot with the correlation time between α_1 and α_2 less than 15 s. Adapted from [55].

ms) reveals α decays from known nuclei (e.g. ^{190}Po, ^{196,197}Rn,...) produced in the studied reaction or in the reactions on heavier samarium isotopes present as impurities in the target. The α peak at 7.7 MeV could be identified as due to α decay of the new isotope ^{194}Rn by using the two dimensional α-α correlation plot. It was constructed by imposing as extra condition that the first α decay (α_1) is followed by a second α decay (α_2) within 15 s in the same position as the α_1 decay. In this way a correlation between the α decay of ^{194}Rn and ^{190}Po / ^{186}Pb and between ^{190}Po and ^{186}Pb could be established. The correlation times were chosen as a compromise between statistics (a few times the half life of the longest lived isotope) and random correlated events.

Essentially the same principles are used in the search for new elements in the region of the Super Heavy Elements (see Sec. 2.4.3). For example, element $Z = 113$ was observed with a cross section as low as 20 fb using cold fusion reaction with ^{208}Pb and ^{209}Bi targets, and $Z = 118$ was identified in fusion reactions using beams of ^{48}Ca on actinide target with cross sections around 0.6 pb [53,58,57].

2.4 Examples of nuclear-structure information extracted from α-decay studies

Recent experiments in the very neutron-deficient isotopes around Z=82 and in the heavy and superheavy element region have considerably expanded the number of α-decaying isotopes. In this section, a number of selected examples where α decay plays an important role will be discussed.

2.4.1 Super-allowed α decay around ^{100}Sn

The α decay of ^{212}Po is a textbook example of 'allowed' α decay as it involves two protons and neutrons just outside the respective shell closures at Z=82 and N=126. From a reduced width [30] or α-particle formation probability [29] point of view (see Fig. 4), it is indeed the fastest α decay observed. However, from the fact that the protons and neutrons occupy different shell-model orbitals, it was conjectured that α decay of nuclei along the N=Z line could be "super-allowed". This is because in the latter case the protons and neutrons occupy the same shell-model orbitals, which could lead to enhanced clustering into an α particle. Thus α-decay studies of nuclei close to ^{100}Sn nucleus reveal interesting information on the nuclear-structure of N=$Z$$\sim$50 nuclei and on the α-decay process itself [59,14].

The peculiar issue with these studies is that, because of the stabilizing effect of the proton and neutron shell closures, the Q_α values of the daughter nuclei increase and thus their half life decrease. This is similar to the region 'north-east' of ^{208}Pb as e.g. illustrated by the sequence: ^{224}Th (E_α=7.17 MeV, $T_{1/2}$=1.05 s) $\rightarrow$ ^{220}Ra (7.45 MeV, 18 ms) $\rightarrow$ ^{216}Rn (8.05 MeV, 45 μs) $\rightarrow$ ^{212}Po (8.79 MeV, 0.3 μs) $\rightarrow$ ^{208}Pb(stable). The same happens around ^{100}Sn where the double α-decay chain ^{110}Xe (3.73 MeV, 105 ms) $\rightarrow$ ^{106}Te (4.16 MeV, 70 μs) $\rightarrow$ ^{102}Sn was reported from a study at the GSI on-line separator [59]. Experiments at the Holifield Radioactive Ion Beam Facility Recoil Mass Spectrometer extended these studies towards the ^{109}Xe (4.06 MeV, 13 ms) $\rightarrow$ ^{105}Te (4.88 MeV, 0.62 μs) $\rightarrow$ ^{101}Sn decay chain [43]. This experiment required special attention to the signal treatment because of the very short-half life of ^{105}Te. This half life is much shorter compared to the typical time processing of silicon detector signals using analog electronics. The latter is of the order of μs due to the shaping applied in analog amplifiers. Thus using these spectroscopy techniques, the α-decay signal from ^{109}Xe would pile up with the one from ^{105}Te. Digital electronics, where the signal traces from the preamplifiers are sampled every 25 ns, allowed to separate these two decays as is shown in Fig. 7. In a follow up experiment, fine structure in the α decay of ^{105}Te was observed and it was concluded that the α line originally assigned to the ground-state to ground-state transition decays in fact towards an excited state at 171.7 keV in ^{101}Sn [44]. This state was already reported from an in-beam γ-ray experiment at the Argonne Fragment Mass Analyser separator [60] and was interpreted as a $7/2^+$ to $5/2^+$ transition, proposing the ground-state spin and parity of ^{101}Sn to be $I^\pi = 5/2^+$. However from the α-decay probability, as determined in [44], it was concluded that the order of two states should be reversed,

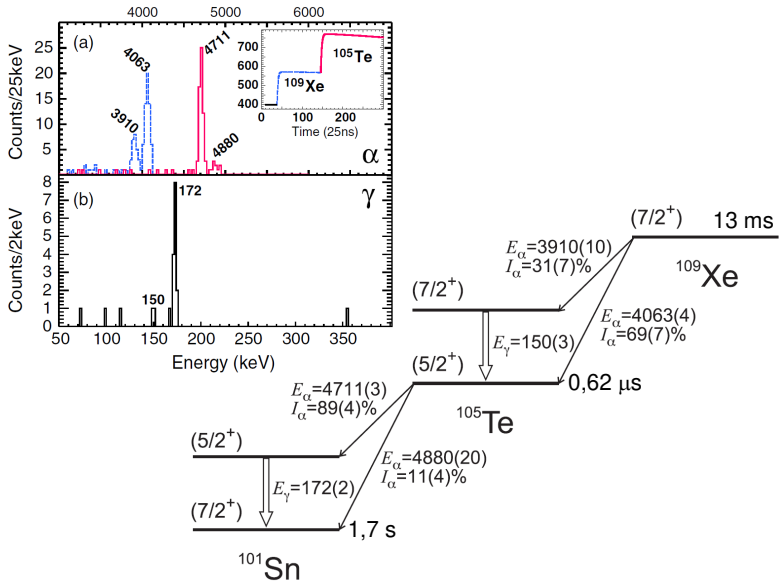

Fig. 7 (Left panel, top) The α-decay energy spectrum obtained after implantation of ^{109}Xe in a DSSD and filtered for double-pulse recording is shown together with an example of a preamplifier trace from the DSSD detector. Recording the full trace allowed to separate the parent from the daughter decay and to determine the α energy precisely. The weak ground-state to ground-state transition at 4880 keV and a much stronger fine structure decay at 4711 keV are marked in the spectrum. The panel below provides the coincident γ-ray spectrum showing evidence for populating the excited level at 171 keV in ^{101}Sn. (Right panel) A partial α-decay scheme for the decay of ^{109}Xe $\rightarrow$ ^{105}Te $\rightarrow$ ^{101}Sn. The fine structure decay of ^{105}Te is strongly suggesting that the structure of the connected states is similar. In contrast, the much smaller intensity of the ground-state to ground-state decay suggests different structures for the parent and daughter states. Adapted from [44].

suggesting an $I^{\pi} = 7/2^{+}$ ground state spin and parity for ^{101}Sn. The order of these two states in ^{101}Sn, one neutron outside the N=50 shell closure, has a profound impact on the nuclear-structure understanding of the ^{100}Sn region as it determines the effective neutron single-particle energy and can discriminate between shell-model calculations using different effective interactions [44,60]. This controversy could possibly be solved using other experimental tools like e.g. laser-spectroscopy studies as described in [61,62].

The reduced α-decay width (see Sec. 2.2 and [30]) of ^{105}Te was compared with the 'equivalent' decay of ^{213}Po (2 protons plus 3 neutrons above the doubly-magic cores of ^{100}Sn and ^{208}Pb, respectively) and an enhancement factor of $\sim$3 was observed hinting to the super-allowed nature of the former decay. Recently this has been interpreted in the framework of a full microscopic shell-model based calculation to analyze the formation probabilities and subsequent α decay of ^{212}Po and ^{104}Te [42]. The calculated α-particle formation probability in ^{104}Te is 4.85 times larger compared to ^{212}Po and thus, based on these results, the α decay towards ^{100}Sn can be considered 'super allowed'.

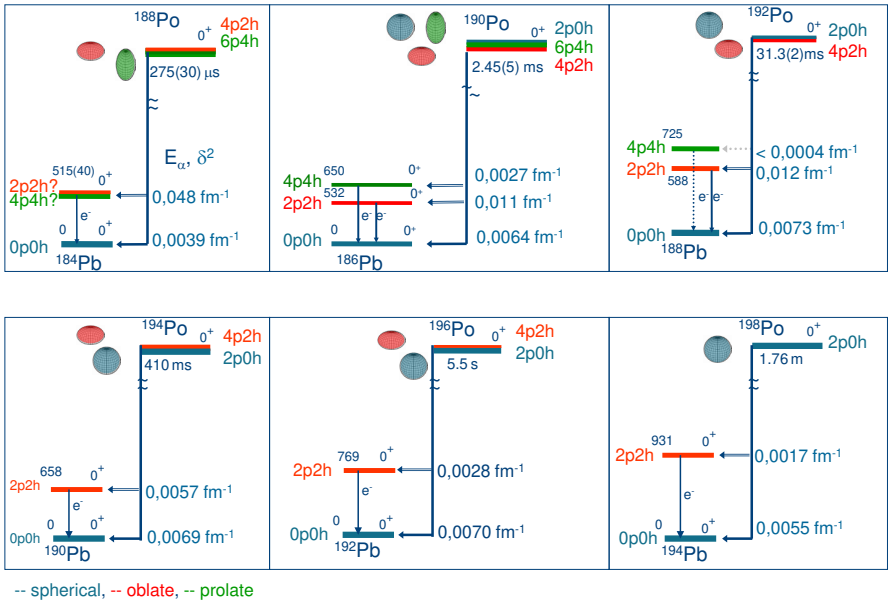

Fig. 8 The results from the α-decay fine structure study of the neutron-deficient even-even $^{188-198}$Po isotopes are shown. These studies revealed the existence of low-lying 0^+ states in the corresponding daughter lead isotopes. In ^{186}Pb it could be shown that the first three excited states have 0^+ spin and parity. The excitation energy of the 0^+ states is given in keV and the half life of the polonium isotopes is shown. Next to the arrows indicating the α-decay branch, the α particle formation probability ($|\mathrm{RF}_\alpha(R)|^2$) is given as calculated following [31,32] (see 20). The color code indicates the nuclear-model dependent interpretation of the deformation of the 0^+ states (see also Fig. 9).

2.4.2 Shape coexistence in the neutron-deficient lead region

Shape coexistence in atomic nuclei is a topic introduced in 1956 by Morinaga [63] when the first excited state at 6,049 MeV in ^{16}O, which has spin and parity $I^\pi=0^+$, was interpreted as a deformed state. The observation of a strongly deformed state in a doubly-magic nucleus came as a big surprise. Its structure was deduced as due to proton/neutron multi-particle multi-hole excitations across the closed proton and neutron shell gaps at $N=Z=8$. Shape coexistence is manifested by the appearance of so-called 'intruder' states with different deformation situated at relatively low-excitation energy in the atomic nucleus. Since the work of [63], shape coexistence has been identified in most regions of the nuclear chart and recent reviews on the subject can be found in [64, 65]. α decay has played an important role in the study of shape coexistence in the neutron-deficient lead region as it allowed, through the study of the fine structure in the α decay of even-even nuclei, to identify and characterize low-lying 0^+ states.

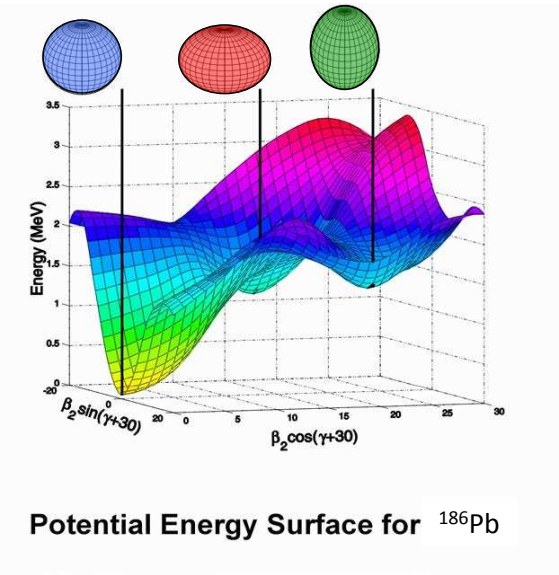

Fig. 9 The total potential energy surface of ^{186}Pb showing three minima in the beta/gamma deformation plane. The minima of the spherical (0p-0h) (blue), oblate (2p-2h) (red) and prolate (4p-4h) (green) shapes are indicated. The 2p-2h and 4p-4h denote the number of protons excited across the $Z = 82$ shell closure, 2 and 4 respectively. Adapted from [67].

For even-even nuclei these are low-lying 0^+ states on top of which collective bands can be build - see e.g. Fig. 1 from [66] where the systematics of the excited states in the even-even mercury isotopes is shown. While these states involve proton multi-particle multi-hole excitation across Z=82, they are situated at low excitation energy due to the gain in pairing energy and extra residual interactions between the valence protons and neutrons. The latter is dominated by quadrupole correlations which induce quadrupole deformation and give rise to the typical parabolic behavior of the excitation energy as a function of valence neutron numbers. In the lead nuclei, it was expected that these shape coexisting states come lowest in excitation energy around N=104 (^{186}Pb) midshell between N=82 and 126.

A study was undertaken at the SHIP velocity filter to investigate the α decay of ^{190}Po to identify and characterize excited 0^+ states in the daughter ^{186}Pb nucleus. The results of this and other studies are shown in Fig. 8. In ^{186}Pb two excited 0^+ states were identified below the first excited 2^+ state making this nucleus unique in the nuclear chart as this is the only nucleus which has three lowest states as 0^+ [67]. By using different types of calculations, like e.g. mean-field, beyond mean-field as well as symmetry based

calculations [64], which provide a robust picture of shape coexistence, the three 0^+ states were interpreted as spherical, oblate and prolate deformed. Fig. 9 shows the calculated total potential energy surface of ^{186}Pb and demonstrates the three minima, that give rise to these three different shapes. The α-formation probability ($|RF_\alpha(R)|^2$) for the individual α decay towards the three 0^+ states could be deduced (see Eq. 2.2) and is indicated in Fig. 8. From this we learn that the $|RF_\alpha(R)|^2$ feeding the excited 0_2^+ state increases over one order of magnitude when going from ^{198}Po to ^{188}Po (see also Fig. 4). Differences in charge radii as deduced from laser spectroscopy studies show that the neutron-deficient lead isotopes stay spherical in their ground states while for polonium the onset of deformation is evidenced for the lightest isotopes [68, 69]. Combining this information with data from in-beam gamma spectroscopy studies in lead and polonium [64, 70] we can infer a gradually stronger mixing of the intruder states in the ground state of the lightest polonium isotopes. This mixing is pictorially represented by the color code of Fig. 8. Dedicated calculations have been performed with a focus on the fine structure observed in α decay in the lead region [71–75]. They show agreement with the data supporting the importance of α decay as a probe for nuclear-structure studies. Further, because of the increased mixing in the polonium ground state [70], the $|RF_\alpha(R)|^2$ value of the ground-state to ground-state α decay of the lightest polonium isotopes is reduced as can be seen in Fig. 4. Finally, the smaller α formation probability of the lightest polonium isotopes to populate the ground state of the corresponding lead isotopes causes the strong deviation of the lightest polonium isotopes from the Geiger-Nuttall rule as seen in Fig. 8 which can now be understood as being due to a nuclear-structure effect.

2.4.3 Searching for the heaviest elements

Studying the heaviest elements at the end of Mendeleev's table impacts different research domains ranging from atomic physics and chemistry, over nuclear physics and nuclear astrophysics [53, 76, 57]. How do relativistic effects influence the electron configuration and thus the chemical properties of the heaviest elements? Where is the end of the periodic table and does the long predicted island of increased stability exist? How does the nucleosynthesis r-process end? These are only a few key questions that are addressed by heavy element research. Recently, the discovery of four new elements have been acknowledged and names and symbols have been given by the International Union of Pure and Applied Chemistry (IUPAC): Nihonium (Nh) for element 113, Moscovium (Mc) for element 115, Tennessine (Ts) for element 117 and, Oganesson (Og) for element 118. In a recent Nobel Symposium NS160, entitled "Chemistry and Physics of Heavy and Superheavy Elements", the field was reviewed and the reader is referred to the individual contributions for a detailed overview of the current state of the art [77].

Because of its high sensitivity to detect decay events of single, individual ions, α decay plays a pivotal role in the discovery and study of the heavy and superheavy elements (see Sec. 2.3). Cold fusion reactions combining projec-

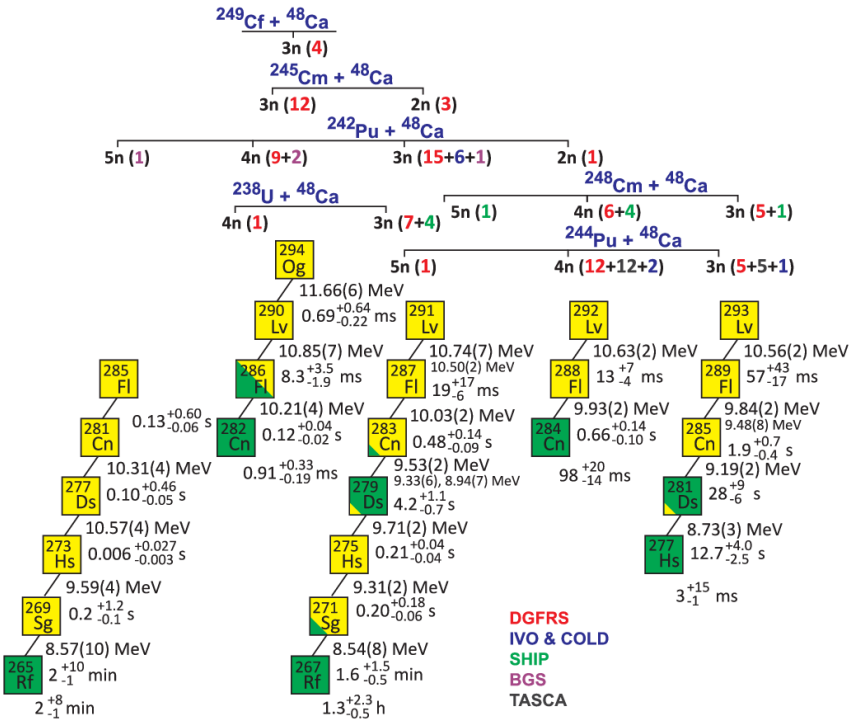

Fig. 10 Different α-decay chains supporting the discovery of the new $Z = 114,116,118$ elements (Fl, Lv and Og, respectively). These were obtained using ^{48}Ca reactions on different actinide targets. The number of decay chains observed in the different experiments is indicated. The color code indicates the facility where the events were identified and the reader is referred to the original paper for further information. The average α-decay energy and half lives are given for the α emitters observed (yellow square). The green squares indicate spontaneously-fissioning nuclei. Figure from [58]

tiles around and above doubly-magic ^{48}Ca with targets of doubly-magic ^{208}Pb (or ^{209}Bi), are used to produce the new elements up to Z=113. These reactions result in low-excitation energy of the compound nucleus and thus to the emission of at most one or two neutrons. The identification of the reaction products could be established using the recoil-α-α time and position correlations method and α-decay chains that link to known regions of the nuclear chart [78]. This is similar to the example of ^{194}Rn shown in Fig. 6. For the discovery of the more heavy elements fusion reactions using ^{48}Ca beams on

long-lived actinide targets (that are more neutron-rich as compared to ^{208}Pb) were used [58]. These reactions lead to higher excitation energies in the compound nucleus and thus to the emission of typically three to four neutrons (hot fusion). Still this results in more neutron-rich isotopes from which the α-decay chains end in so-far unknown spontaneously fissioning nuclei (see Fig. 10). Therefore, often, other means as e.g. cross bombardment with different beam/target combinations (see Fig. 10) and measurements of excitation functions have to be used to firmly establish the Z and A of the newly discovered element and isotope.

The fact that α-decay energies can be determined with good accuracy (typical up to a few tens of keV uncertainty) allows to deduce accurate masses and binding energies of these heavy isotopes provided the mass of one of the isotopes in the α-decay chain is measured with good accuracy. Penning trap mass spectroscopy is an excellent tool to measure absolute values of atomic masses [79] and it has been applied to the heavy mass region measuring $^{252-254}$No ($Z = 102$) [80,81]. These measurements revealed new masses and binding energies for a wide range of isotopes giving information on the deformed shell closures around N=152 and N=162 [81]. Other mass spectroscopic techniques like multi-reflection time of flight mass spectrometer (MR-ToF-MS) have recently been commissioned and are now used in the super heavy element region [82]. It should be noted, however, that the use of α-decay energies to link isotopes with accurately known mass with other isotopes only works if the ground-state to ground-state α-decay energy is known. While the latter is obvious for even-even isotopes as their α decay is dominated by the 0^+ - 0^+ α decay, it is less obvious for odd mass and odd-odd isotopes. Because of the fine structure in the α decay of most nuclei and of the potential presence of long living isomers, it might not be possible to extract the ground-state to ground-state α-decay energy from the α spectra. Therefore detailed α-γ spectroscopy studies are necessary [83]. In turn, through these fine-structure α-decay studies excited states can be identified and their characteristics determined. The latter data serve as important input to improve theoretical models and to make predictions more reliable [84].

3 Beta-delayed fission

3.1 Introduction to low-energy fission

Nuclear fission, discovered in 1938 [5], provides one of the most dramatic examples of nuclear decay, whereby the nucleus splits preferentially into two smaller fragments releasing a large amount of energy [85,86]. Fig. 11(a) shows the simplified concept of the fission process within the so-called macroscopic 'Liquid Drop Model' (LDM), as used in 1939 to explain fission [6]. The nuclear potential energy surface (PES) for a ^{238}U nucleus is shown as a function of two important parameters in fission: elongation (e.g. quadrupole deformation) of the initial nucleus and the mass asymmetry of resulting fission fragments.

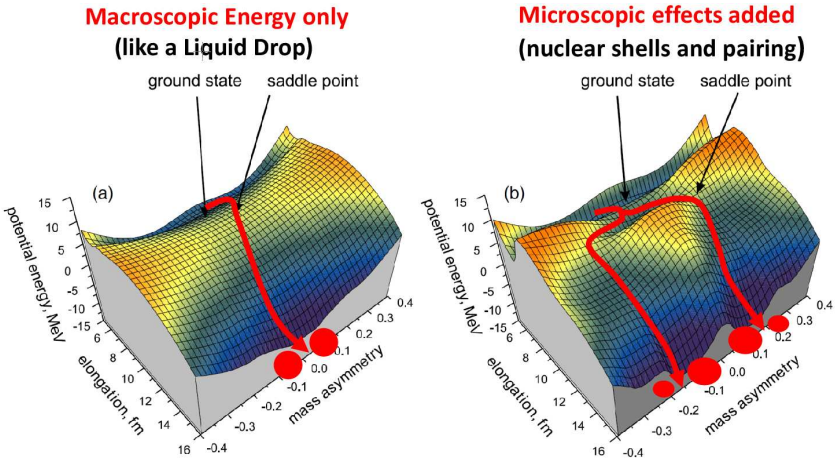

Fig. 11 (Color online) a) Macroscopic, $V_{\rm macro}$(LDM), and b) total, $V_{\rm total} = V_{\rm macro}$(LDM)+$V_{\rm micro}$(Shells) potential energy surface for the ^{238}U nucleus as a function of elongation and fission-fragment mass asymmetry. The most probable fission paths (or 'fission valleys'), which follow the lowest energy of the nucleus, are shown by the red lines with arrows. While in the LDM approach only symmetric fission can happen along the single 'symmetric' valley, the introduction of microscopic shell effects produces the asymmetric fission valleys. The mass asymmetry parameter is defined as the ratio $\frac{A1-A2}{A1+A2}$, where $A1$ and $A2$ are masses of the two fission fragments (thus, the mass asymmetry =0 for symmetric mass split). The energy difference between the ground state and the saddle point defines the quantity, dubbed as 'fission barrier height'. Figure modified from [87].

Within the LDM, the nucleus elongates along the line of zero mass asymmetry during the fission process. This is shown as a red line in Fig. 11(a). Thus, initially the nucleus increases its potential energy, until at some moment the maximum of the potential energy surface is reached. This point is called the saddle point (the top of the fission barrier). Afterwards, at even further elongation, the nucleus reaches the scission point and splits in two equal fission fragments.

While the classical LDM was able to qualitatively explain why fission is one of the important decay modes of heavy nuclei, it failed to describe e.g. the experimentally-observed asymmetric mass split in two un-equal fragments, which was realised already in 1938. Following the recognition of the importance of the microscopic shell corrections, which arise due to specific/non-uniform occupancies of levels by protons and neutrons, the description of the fission process was discussed within the so-called macroscopic-microscopic

framework [88–90]. In this model, the total potential energy becomes the sum of macroscopic (LDM) and microscopic shell effects (Shells) energy: $V_{\rm total} = V_{\rm macro}({\rm LDM}) + V_{\rm micro}({\rm Shells})$. This naturally led to the appearance of the asymmetric fission valleys on the potential energy surface (see, Fig. 11(b)), thus to the asymmetric fission-fragment mass distribution (FFMD).

Therefore, fission is a unique tool for probing the nuclear potential-energy landscape and shell effects at extreme values of deformation, and as a function of mass asymmetry, spin, and excitation energy. In particular, fission enables the study of nuclear-structure effects in the heaviest nuclei [91], has direct consequences on their creation in nuclear explosions [92] and in the astrophysical r-process [93–95]. The latter is terminated by fission, thus fission has a direct impact on the abundance of medium-mass elements in the Universe through so-called "fission recycling". The fragments, resulting from fission of very heavy nuclei, become the new seed nuclides for the r-process. Apart of its importance for fundamental studies, fission has many practical applications, such as the generation of energy and the production of radioisotopes for science and medicine. Fission is also a very powerful mechanism to produce nuclei far from the stability line [96].

It is important to note the strong dependence of microscopic effects on the temperature (or, excitation energy) of the nucleus. Indeed, the shell effects are 'washed out' at sufficiently high excitation energies, which leads to the disappearance of asymmetric fission valleys on the potential energy surface, reverting it to the smooth LDM-like surface, as shown in Fig. 11(a). Therefore, the nucleus will again fission symmetrically. This explains the strong need for fission studies as a function of excitation energy, and also as a function of proton and neutron number to reveal specific nuclear-structure effects on fission.

As a function of the excitation energy of the fissionning nucleus, the fission process is often broadly classified either as high-energy fission, in which the excitation energy strongly exceeds the fission barrier height, or as low-energy fission. In contrast to high-energy fission, in which the microscopic effects are washed out, the interplay between macroscopic and microscopic effects in fission can be sensitively explored at low excitation energy. In particular, in spontaneous fission (SF) from the ground state, the excitation energy is $E^* = 0$ MeV, while in SF from isomeric states or in thermal neutron-induced fission it does not exceed a few MeV [85]. However, being the ultimate tool for low-energy fission studies, SF is limited to heavy actinides and trans-actinides [97]. Recently, by using Coulomb excitation (often dubbed as "Coulex") of relativistic radioactive beams, fission studies became possible in new regions of the Nuclidic Chart, earlier unexplored by low-energy fission [98,99], see Sec. 3.5.4. In this case, the excitation energy is centered around $E^* \sim 11$ MeV. In terms of the excitation energy, the beta-delayed fission (βDF), which is the topic of this section, is intermediate between SF and Coulex-induced fission. As will also be shown below, βDF allows to study low-energy fission of some of the most exotic nuclides, which are not yet accessible to fission studies by

other techniques, and which do not fission spontaneously from their ground state.

3.2 Mechanism of beta-delayed fission, conditions to occur, observables

The exotic process of β-delayed fission can be considered as a sub-class of a more general group of beta-delayed decay processes, which includes β-delayed proton (denoted βp), β-delayed neutron (βn), β-delayed gamma ($\beta\gamma$) and β-delayed α particle ($\beta\alpha$) emission, see detailed reviews [100, 101]. All these decay modes proceed via two steps, first the β (β^+/EC or β^-) decay happens, which can be accompanied, under certain conditions, by the subsequent emission of one of the particles (or more particles, in case of multiparticle β-decay processes, e.g, β2n for β-delayed two neutron emission). Similarly, β-delayed fission, discovered in 1965 – 1966 [102–104] is a two-step nuclear-decay process that couples β decay and fission. In these lecture notes we will review the most salient features of βDF and discuss some of the most recent methods and results, while we refer the reader to a comprehensive review [105] for a detailed discussion of this topic.

In βDF, a parent nucleus first undergoes β decay, populating excited state(s) in the daughter nuclide. In the case of neutron-deficient nuclei, electron capture (EC) or β^+ decay is considered (referred further as β^+/EC), while β^- decay happens on the neutron-rich side of the Nuclidic Chart. Fig. 12 shows a simplified diagram of βDF for the case of neutron-deficient nuclei, which are mostly considered in this study. If the excitation energy of these states, E^*, is comparable to or greater than the fission barrier height, B_f, of the daughter nucleus ($E^* \sim B_f$), then fission may happen in competition with other decay modes, e.g. γ decay and/or particle emission (neutron, proton or α), depending on which side of the β-stability valley the parent nucleus is situated. Therefore, the special feature of βDF is that fission proceeds from excited state(s) of the daughter nuclide, but the experimentally-observed time behavior of the βDF events is determined by the half-life of the parent nucleus (as with any β-delayed particle decays). As in most cases the β-decay half-lives are longer than tens of ms, it makes βDF more easily accessible for experimental studies. The experimental observables from βDF include: half-life, probability ($P_{\beta DF}$, see Sec. 3.6), kinetic energies of resulting fission fragments, and energies and multiplicities of e.g. γ rays and neutrons, accompanying the fission process. It is important to stress that the unique experimental signature for βDF is the coincidences between the x rays (usually, K x rays) of the *daughter* nucleus (which arise after the EC decay of the parent) with the fission fragments. This method was used by the Berkeley group in some of their experiments to directly confirm the βDF process in e.g. ^{232,234}Am [106–108] and in ^{228}Np [109].

Two main conditions must be satisfied for βDF to occur in measurable quantities. First of all, the parent nucleus must possess a non-zero β-branching ratio ($b_\beta > 0$). Secondly, the Q_{β^-}-value of the parent must be comparable to or

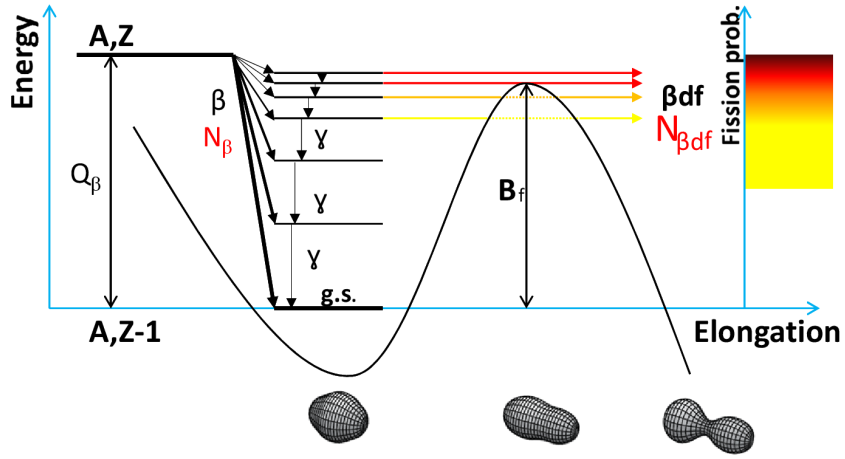

Fig. 12 (Color online) Schematic representation of the βDF process on the neutron-deficient side of the nuclear chart. The Q_β value of the parent (A, Z) nucleus is indicated, while the curved line shows the potential energy of the daughter $(A, Z-1)$ nucleus with respect to nuclear elongation. The fission barrier B_f is also shown. The color code on the right-hand side represents the probability for excited states, with excitation energies close to B_f, to undergo fission; the darker colors correspond to higher probabilities. The plot is from [110].

be higher than the fission barrier of the daughter $Q_{\beta^-}(\text{Parent}) \sim B_f(\text{Daughter})$. These conditions are fulfilled for three regions of nuclei a) very neutron-deficient isotopes in the lead region (see Secs. 3.5.1–3.5.3), b) very neutron-deficient nuclides in the neptunium-to-mendelevium (Np–Md) region, and c) very neutron-rich isotopes between francium and protactinium. In these three regions, βDF was indeed experimentally observed.

Historically, βDF studies were performed first for the neutron-deficient nuclei in the uranium region, as a by-product of extensive searches for new elements in the 1960'ies. Since the EC decay dominates over the β^+ decay in these cases, the term EC-delayed fission (ECDF) was often used in the literature, while the term βDF was predominantly reserved for β^--delayed fission in the neutron-rich nuclei. However, since in the neutron-deficient lead region the β^+ decay can effectively compete with the EC decay, we will use throughout this review the term βDF for both the neutron-rich and neutron-deficient nuclei.

A distinctive feature of βDF is its *low-energy* character. Previously, low-energy fission studies were limited to nuclei along the valley of stability from around thorium (Th) to rutherfordium (Rf) and above, mostly using SF and

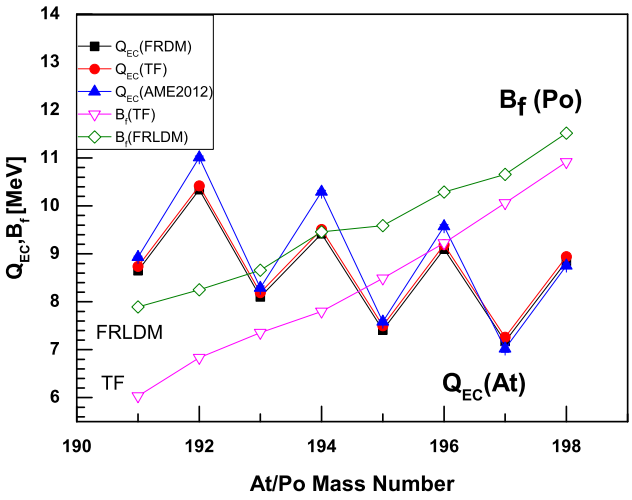

Fig. 13 (Color online) Calculated Q_{EC}(At) (closed circle and square symbols) and B_f(Po) (open symbols) values from the FRDM/FRLDM [113,114] and from the TF model [115]. The Q_{EC} values from AME2012 [17] are shown by the closed triangles. The plot is from [116].

fission induced by thermal neutrons. In βDF, the *maximum* excitation energy of the daughter nucleus is limited by the Q_{EC} (Q_{β^-} in case of neutron-rich nuclei) of the parent nuclide. The typical Q_{EC} (Q_{β^-}) values are in the range of 3 – 6 MeV and 9 – 12 MeV for the known βDF nuclei in the trans-uranium and lead regions, respectively.

The importance of βDF is also highlighted by its ability to provide low-energy fission data for very exotic nuclei which do not decay by SF and which are difficult to access by other techniques. For example, the recently-studied βDF nuclei in the lead region possess very different neutron to proton ratios, e.g. $N/Z = 1.23 - 1.25$ for ^{178,180}Hg (see Section 3.5.1) in contrast to a typical ratio of $N/Z = 1.55 - 1.59$ in the uranium region, where numerous SF and βDF cases were long-known. This allows to investigate potential differences in the βDF process and its observables in the two regions, which differ in many nuclear-structure properties, see discussion in Secs. 3.5.1–3.5.3.

Finally, the potential role of βDF for the r-process termination by fission (along with neutron-induced and spontaneous fission) is the subject of on-going discussion [93–95], also in view of its possible implications for the determination of the age of the Galaxy by the actinide geochronometers [111, 112].

We refer the reader to Tables 1 from [105,110] where all 26 βDF nuclei, known by 2013, are summarized. In [105] a review of production/identification methods and of the βDF probability values is provided, while [110] discusses

the partial βDF half-lives. Since then, three new βDF nuclides - ^{230}Am, ^{236}Bk and ^{240}Es were discovered, see Sec. 3.4. The data, shown in these tables, demonstrate that so far all known βDF emitters are odd-odd nuclei. To explain this point and to highlight common phenomena relevant to βDF, we analyse in Fig. 13 an example of βDF of neutron-deficient At isotopes. The calculated Q_{EC}(At) and B_f(Po) values in the region of our interest for the Finite Range Droplet Model/Finite Range Liquid Drop Model (FRDM/FRLDM) [113,114] and for the Thomas-Fermi (TF) model [115] are compared to the extrapolated or experimental Q_{EC}(At) values from Atomic Mass Evaluation (AME2012) [17]. However, the latter values should be considered with caution since in most of the lightest odd-odd astatine isotopes, e.g. in ^{192,194}At [117,118], there are more than one long-lived nuclear state with unknown relative excitation energy and β-branching ratios. Furthermore, it is not always known which of them is the ground state and for which the experimental mass determination was quoted. This is a quite general issue in the odd-odd nuclei, which might influence the derivation of fission fragments mass distributions and probability values in βDF studies.

A few important features are evident in Fig. 13. First of all, the good agreement for the Q_{EC}(At) values between the two mass models is most probably because the Q_{EC} values are deduced as a difference of the calculated parent and daughter masses. Therefore, even if the two models give masses, systematically shifted by some value, this shift will largely cancel out in their difference.

Secondly, due to the odd-even staggering effect in masses, the Q_{EC} values of the odd-odd (thus, even-A) parent astatine isotopes are on average $\sim 1.5-2$ MeV larger than for their odd-A neighbors. This is one of the main reasons why so far all nuclei where βDF was observed experimentally are odd-odd. Another reason is that after the β decay of an odd-odd isotope, an even-even daughter is produced, which is expected to fission easier than an odd-A neighbor, produced after the β decay of an odd-A precursor. The very strong (several orders of magnitude) hindrance for SF of the odd-A and odd-odd nuclei in comparison with the even-even nuclides is a well-established experimental fact, see e.g. [97]. As the excitation energy of the fissioning daughter nucleus in βDF is relatively low, similar fission hindrance factors could be also expected for βDF, however this is still an open question.

Another important feature shown in Fig. 13 is that while both models predict a fast decrease of the calculated fission barriers as a function of lowering neutron number, the rate of decrease is different. As a result, the respective calculated Q_{EC}(At) - B_f(Po) values are quite different, e.g. -0.08 MeV (FRDM/FRLDM) and +1.7 MeV (TF) for ^{194}At. Thus, one could expect that the chance of β-decay feeding to states in the vicinity or above the fission barrier in the daughter ^{194}Po should be higher in the TF model in comparison to FRDM/FRLDM model, however the specific β-decay strength function needs to be considered, see Sec. 3.6. For ^{198}At, both models predict large negative Q_{EC}(At) - B_f(Po) values, thus only sub-barrier fission of ^{198}Po can happen, which will most probably result in negligible/unmeasurable βDF probability.

On the other hand, both models predict large positive Q_{EC}(At) - B_f(Po) values for ^{192}At, thus higher probabilities are expected in this case, which was indeed confirmed in the SHIP experiments [119]. A similar effect occurs for several βDF cases in the lead region, as discussed for ^{178}Tl [120], ^{186,188}Bi [121] and ^{196}At.

Several βDF studies explored the sensitivity of βDF probability values to the Q_{EC} - B_f differences, to infer information on the fission barrier height [122–125], thus to check the validity of different fission models far from the β-stability line, this will be discussed in Sec. 3.6.

3.3 Production of βDF nuclei and determination of their properties

Historically, four methods were exploited to produce nuclei which exhibit the βDF decay, they are described in more details in review [105].

– Charged-particle induced reactions, typically fusion-evaporation or transfer reactions at beam energies in the vicinity of the Coulomb barrier. E.g. the first βDF cases in ^{228}Np and ^{232,234}Am were identified in the fusion-evaporation reactions ^{10,11}B+^{230}Th$\rightarrow^{232,234}$Am and ^{22}Ne+^{209}Bi$\rightarrow^{228}$Np [102,103].
– Reactions induced by γ rays and neutrons, see e.g. [126,127].
– Radiochemical separation from naturally-occurring long-lived, usually neutron-rich, precursors, see e.g. [126,128].
– Spallation reactions with 1-GeV protons on a thick uranium target, followed by mass separation with an electromagnetic mass-separator [9]. The recent novel experiments at the ISOLDE mass separator at CERN (Geneva) [48] used the same method to identify βDF of ^{178,180}Tl [129,120,130], ^{194,196}At [119] and ^{200,202}Fr [131], they will be discussed in details below.

In the earlier βDF experiments in 1960-1980'ies, which mostly exploited the first two production methods described above, rather simple 'mechanical' techniques, e.g. the rotating drum or a thick catcher foil [132] were used to collect *all* reaction products for subsequent observation of their decays. The main drawbacks of such experiments were discussed in [105] and are briefly summarized here. First of all, many other reaction channels can be open, including those involving possible impurities in the target, which could produce other nuclei, that possess a fission branch (e.g. SF). Therefore, in the absence of direct determination of A and/or Z of the fissionning parent nucleus, the assignment of the observed activity to βDF to a specific isotope could often be ambiguous. To partially overcome this issue, a tedious series of cross-bombardments to produce the same βDF candidate in different projectile-target combinations had to be performed, also as a function of the projectile energy, to obtain the so-called excitation functions, see e.g. [133]. The latter can be used to differentiate between different reaction channels.

The chemical separation of the element of interest from the collected sample (e.g. from the catcher foil) in some experiments allowed both to get a purer

sample and to achieve the Z-value determination of the fissioning parent nucleus, see e.g. [108]. The use of He-jet technique to transport the fissionning activity from the target region with high radiation levels to a detection system situated some distance (meters) away in a shielded environment is another common method to reduce the background to measure rare decay events [108, 134].

On the detection side, often the so-called mica foil detectors were used in the earlier experiments to register fission events [132]. Such detectors allow to measure the fission rate (thus, production cross sections/excitation functions) and also half-lives of the fissionning activities. However, mica foils fully lack information on the kinetic energy of coincident fission fragments, thus e.g. FFMD's measurements were impossible, as they require the detection of coincident events.

The use of silicon detectors in the earlier experiments was not wide-spread, and at most only single silicon detectors were used. This prohibited the measurements of coincidence fission fragments. From the mid-90'ies, more complex arrangements of silicon detectors, e.g. the merry-go-around detection system at Berkeley [135,136], were introduced in fission research, which provided coincidence measurements of fission fragments.

From the mid-90ies, the use of kinematic separators (see Sec. 2.3) to study the decay of heavy elements and, in particular, of βDF was introduced, see an example of βDF study of ^{194}At in Fig. 14 and Sec. 3.4. The use of ISOL-type separators for βDF studies in the lead region, e.g. ISOLDE at CERN, was introduced since the last decade and brought substantial progress to βDF studies in the lead region, see Sec. 3.5.

3.4 Recent βDF results at recoil separators

Here we will discuss the βDF study of ^{194}At performed at SHIP as one example of βDF studies at recoil separators. The principles of radioactive ion beam production and identification at SHIP were briefly explained in Sec. 2.3. Fig. 14 shows the identification of βDF of ^{194}At [119]. Despite its success, this study also demonstrated several drawbacks of the present βDF experiments at recoil separators. Indeed, 66 fission events were clearly identified in the experiment at SHIP, see Fig. 14(b). However, the interpretation of these decays was hindered due to the presence of two states in ^{194}At with similar half-lives of 310(8) ms and 253(10) ms [118] with yet unknown β-decay branchings. Therefore, the assignment of the observed fission events to a specific (or to both) isomeric states in ^{194}At is not yet clear, see detailed discussion in [119]. Another drawback of such experiments is that the parent nuclei are implanted in the silicon detector at a depth of several micrometers. This prevents an accurate measurement of the individual energies of the coincident fission fragments, as the fission fragment escaping the PSSD detector in the backward hemisphere leaves some of its energy in the PSSD. This energy will be summed up with the energy of the second fission fragment stopped in the PSSD. Therefore, the

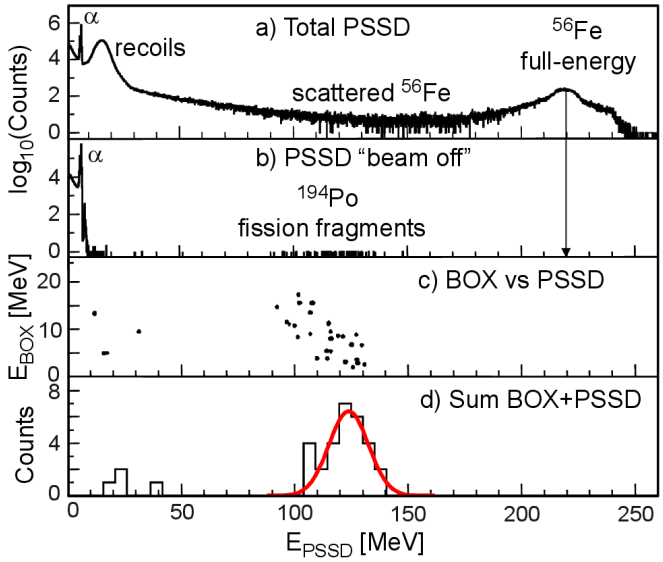

Fig. 14 Identification of βDF of ^{194}At at SHIP in the reaction ^{141}Pr(^{56}Fe,3n)^{194}At. a) The total energy spectrum in the PSSD. The primary beam is provided with a pulsed structure of 5 ms 'beam on' / 15 ms 'beam off', the spectrum shows all data, with no condition on the beam. Note the α decays around 5 MeV, the recoiling nuclei around 20 MeV. The spectrum at higher energies is dominated by the ^{56}Fe beam that leaks through SHIP or is scattered on its way to the PSSD. (b) same as (a) but obtained solely during the 15 ms 'beam off' period. Note the very strong suppression of the primary ^{56}Fe beam and the recoils. Only the α spectrum as well as events due to beta-delayed fission of ^{194}At remain. (c) Two dimensional E_{BOX} versus E_{PSSD} of coincident events detected in the PSSD and in the BOX detector. The group of events in the middle of the plot corresponds to detection of coincident fission fragments, whereby one of the fragments is registered in PSSD, while the second (escaping) fragment - in the BOX detector. (d) The sum energy E_{PSSD}+E_{BOX}, providing the TKE determination for the fission of daughter nuclide ^{194}Po. A Gaussian fit is shown by the red solid line. Adapted from [119].

measured energies of coincident fission fragments in the PSSD and BOX will be distorted, depending on implantation depth and fission fragments angle relative to the detector surface. There is no clear procedure how to account for these effects. As a result, no FFMD's derivation is yet possible in such experiments, as it requires the knowledge of unperturbed kinetic energies of both fission fragments. This is because, in the first approximation, the ratio of fission fragments masses is inversely proportional to the ratio of their kinetic energies. Only information on total fission kinetic energy (TKE) with a rather large uncertainty can be extracted via a tedious calibration procedure, see Fig. 14(d).

Using the same method, 23 βDF events of two isomeric states in ^{192}At were identified at SHIP [119], with similar difficulties encountered with respect of their assignment to a specific isomeric state, as in case of ^{194}At.

The difficulty of isomer separation can, however, be overcome by using the technique of laser-assisted isomer separation, as discussed in the next section.

To conclude this section, we mention that recently, βDF of ^{236}Bk and ^{240}Es was identified at the gas-filled separator RITU at JYFL [137], while βDF of ^{230}Am was observed at the GARIS gas-filled separator at RIKEN [138,139]. For ^{236}Bk and ^{240}Es, quite large βDF probabilities, of the order of $\sim$10% were derived, while a lower limit of $P_{\beta DF}$>30% was derived for ^{230}Am. The latter value is the highest so far among all measured βDF probabilities. Both experiments used a technique, very similar to the SHIP study, but employed more advanced multi-strip DSSSD's.

3.5 A new approach to study βDF at the ISOLDE mass separator at CERN

About a decade ago, a new technique to study βDF nuclei in the lead region was developed at the mass separator ISOLDE [48], by using low-energy 30 – 60 keV radioactive beams. This method allows to extend low-energy fission studies to very exotic neutron-deficient and neutron-rich nuclei, which are difficult to access by other techniques.

As an example, Fig. 15 provides a brief overview of the production method of the isotope ^{180}Tl in the pilot βDF study at ISOLDE [129]. A novel and unique feature of this βDF experiment was the combination of Z-selective ionization of a specific element (Tl, in this case) with RILIS [140,141,9] and subsequent mass separation at $A = 180$ with ISOLDE. After selective ionization, acceleration up to 30 keV, and mass separation, a pure beam of ^{180}Tl with an intensity of $\sim$150 ions/s was analyzed by the Windmill (WM) detection system [129]. Here, the radioactive beam was deposited on a thin carbon foil, surrounded by two silicon detectors (Si1 and Si2), along with HPGe detectors for coincident particle–γ-ray measurements. The use of two silicon detectors in a compact geometry allowed both singles α/fission decays and double-fold fission-fragment coincidences to be efficiently measured. The same method was later used for βDF studies of ^{178}Tl [120], ^{194,196}At [131,116] and of ^{200,202}Fr [131]. A detailed discussion of the results will be given in Section 3.5.3.

The uniqueness of this technique is the unambiguous A and Z identification of the precursor, via the combination of the Z–selection by the RILIS and the mass-separation by ISOLDE. Other advantages include a point-like radioactive source, the implantation in a very thin foil whereby both fission fragments can be efficiently measured with little deterioration of their energies, and the proximity of germanium detectors for γ-ray spectroscopy. Simultaneous measurement of fission and α decays in the same detectors removes some of the systematic uncertainties for branching ratio determination.

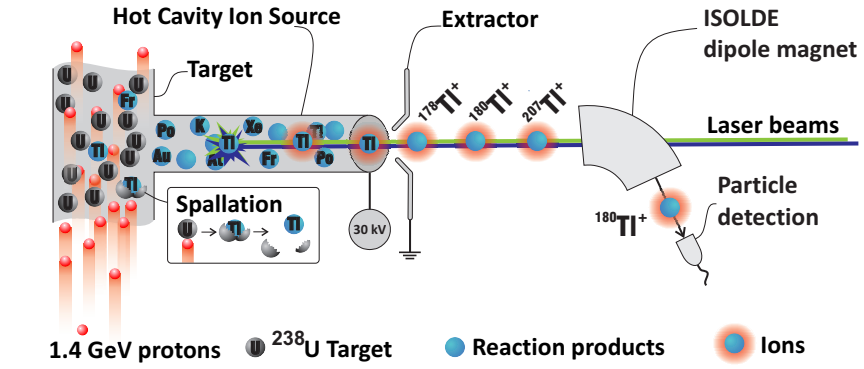

Fig. 15 (Color online) Schematic view of the ISOLDE and Resonance Ionization Laser Ion Source (RILIS) operation as applied in the βDF study of ^{180}Tl [129]. The 1.4-GeV 2 μA proton beam impinges on a thick 50 g/cm^2 ^{238}U target, producing a variety of reaction products via spallation and fission reactions. The neutral reaction products diffuse towards the hot cavity, where the thallium atoms are selectively ionized to the 1^+ charge state by two overlapping synchronized laser beams, precisely tuned to provide thallium ionization in a two-color excitation and ionization scheme. The ionized thallium ions are extracted by the high-voltage potential of 30 kV, followed by the $A = 180$ mass separation with the ISOLDE dipole magnet. The mass-separated ^{180}Tl ions are finally implanted in the carbon foils of the Windmill system (see Fig. 16), for subsequent measurements of their decays with the silicon and germanium detectors, as described in the main text. Plot modified from [142].

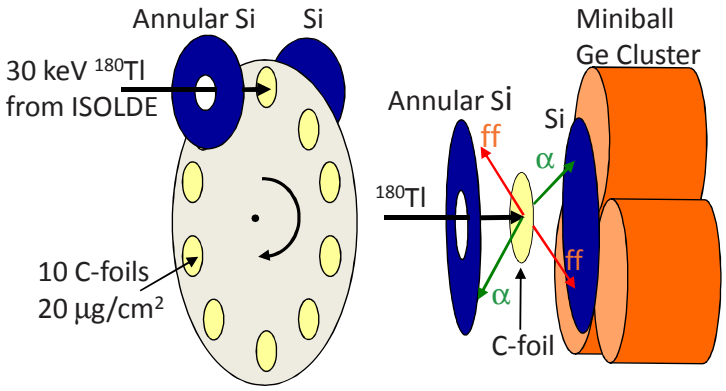

Fig. 16 Left side: The Windmill setup used in the experiments at ISOLDE to study βDF of ^{178,180}Tl, ^{194,196}At and ^{200,202}Fr; right side: a zoom of the detector arrangement. The case of ^{180}Tl is shown as an example, with mass-separated ^{180}Tl ions being implanted through a hole in an annular silicon detector (300 μm thickness) into a thin carbon foil of 20 μg/cm^2 thickness. A second Si detector (300 μm thickness) is placed 3 mm behind the foil. A set of Ge detectors is used for γ- and K X-ray measurements in coincidence with particle decays. Plot is taken from [129].

3.5.1 New island of asymmetric fission in the neutron-deficient mercury region: the case of ^{180}Tl

In this section, as an example of what can be learned from βDF studies, the results of the βDF experiments at ISOLDE will be discussed, in which βDF of ^{178,180}Tl [129,66,120], ^{194,196}At [119,116] and ^{202}Fr [131] was studied, resulting in the low-energy fission data for daughter (after β decay) isotopes ^{178,180}Hg, ^{194,196}Po and ^{202}Rn, respectively.

Historically, the first βDF study at ISOLDE was performed for the isotope ^{180}Tl, whose production method was described in Sec. 3.5. The $Q_{EC}(^{180}\text{Tl}) = 10.44$ MeV and the calculated fission barrier is $B_f(^{180}\text{Hg}) = 9.81$ MeV, thus $Q_{EC}(^{180}\text{Tl})$-$B_f(^{180}\text{Hg}) = 0.63$ MeV, which allows for some above-barrier fission to happen. Despite this, a rather low βDF probability of $P_{\beta DF}(^{180}\text{Tl}) = 3.2(2)\times10^{-5}$ was deduced [105].

In a $\sim$50-hour long experiment, 1111 singles and 356 coincidence fission events were observed and attributed to the βDF of ^{180}Tl, see Fig. 17. The mass distribution for fission fragments of ^{180}Hg is clearly asymmetric with the most abundantly-produced fragments being ^{100}Ru and ^{80}Kr and their neighbors. No commonly-expected symmetric split in two semi-magic ^{90}Zr (Z =40, N =50) nuclei was observed, and the observation of "new type of asymmetric fission in proton-rich nuclei", which differs from asymmetric fission in the trans-uranium region, was claimed [129,143].

3.5.2 Mass-asymmetry in ^{180}Tl and in ^{238}U - what is the difference?

This discovery caused an intense interest from the theory community, whereby very different approaches, such as the macroscopic-microscopic model [129, 143,144], two modern versions of the scission-point model [145–148] and two fully self-consistent models, HFB-D1S and HFB-SkM* [149,150], were used to shed light on the observed phenomenon.

In particular, the five-dimensional (5D) macroscopic-microscopic model [143,151] was first to be applied to explain the observed asymmetric mass split of the fission fragments of ^{180}Hg. Fig. 18 from [143] shows two-dimensional potential-energy surfaces (PES) for ^{180}Hg and ^{236}U and highlights the crucial differences in the nature of asymmetric fission for proton-rich nuclei in the lead region compared to the more classical region of asymmetric fission in the actinide region around ^{236}U.

The PES for ^{236}U shows features common to many actinide nuclei with $226 \leq A \leq 256$, such as a deformed ground state, a relatively low two- or three-humped fission barrier, and most prominently, well-separated symmetric ($\alpha_g = 0$) and asymmetric ($\alpha_g \sim 0.2$) valleys. The latter valley is usually attributed as being due to the strong shell effects (spherical and/or deformed) of fission fragments in the vicinity of the double-magic ^{132}Sn. Fission starts from the ground state on the left-hand side of the figure, passes through the nearly symmetric first saddle point to the symmetric fission isomer minimum around $q_2 \sim$2. Then the mass asymmetry begins to increase as the nucleus passes over

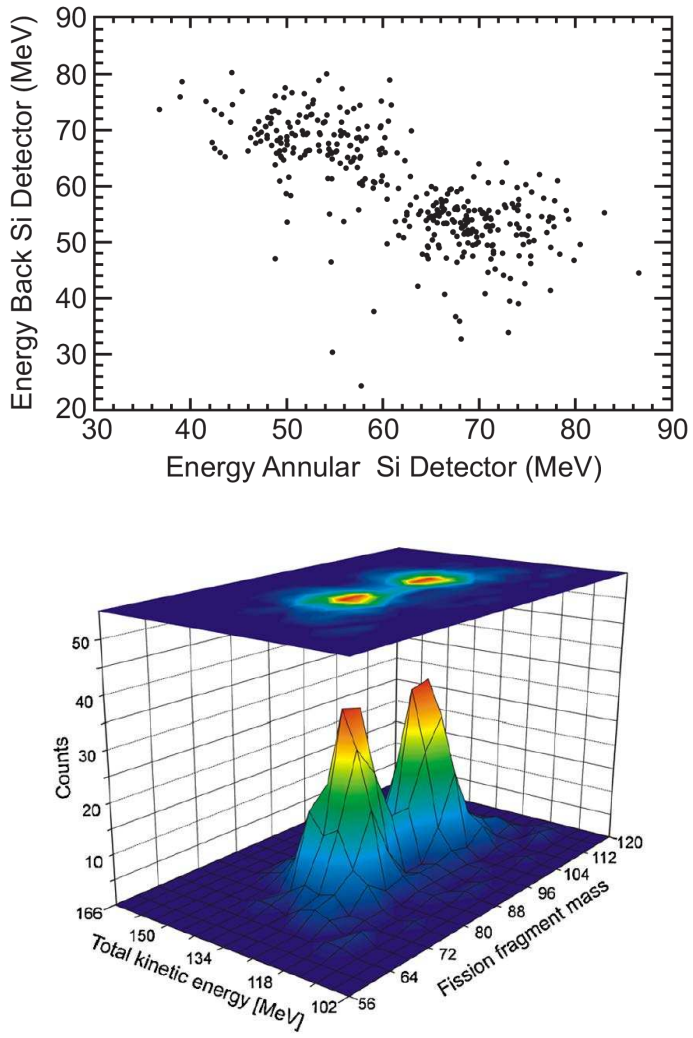

Fig. 17 Top panel: a coincidence energy spectrum for βDF of ^{180}Tl measured by two silicon detectors of the Windmill setup. The two-peaked structure originates because the two fission fragments have different energies, a direct result of the asymmetric mass distribution; Bottom panel: The derived fission-fragment distribution of the daughter isotope ^{180}Hg as a function of the fragment mass and the total kinetic energy. The conversion from energy to mass spectra relies on the conservation of mass and energy, and assumes that the masses of fission fragments add up to the mass of the parent nucleus, see details in [129]. Plots are taken from [129,130].

the mass-asymmetric second saddle point, through a shallow third minimum, and finally over a third asymmetric saddle at the head of the asymmetric valley to a shape near the asymmetric scission point The higher symmetric saddle point reduces the probability of entering the symmetric valley by requiring barrier penetration for systems with near-threshold energies.

In contrast, the PES for ^{180}Hg is very different, with only a single pronounced symmetric valley corresponding to separated semi-magic ^{90}Zr nuclei, and no deep asymmetric valley extending to scission. The dominant symmetric valley is, however, inaccessible due to the high barrier along the symmetric path from the ground state. The symmetric valley remains separated from a shallow asymmetric valley by a high ridge in the potential. It is important to note that, within this model description, by the time the separating ridge disappears, a quite well-defined mass-asymmetric di-nuclear system has already developed with two nascent fission fragments still connected by a narrow neck. However, such a system does not have the possibility for mass equilibration towards an energetically more favorable mass-symmetric split, due to the very small neck size at this moment.

A similar result can also be seen in Fig. 19, which shows the PES calculations within the HFB-SKM* approach [150]. This plot nicely demonstrates the difference between the asymmetric fission of ^{180}Hg and nearly symmetric fission of ^{198}Hg, which is known from earlier experiments.

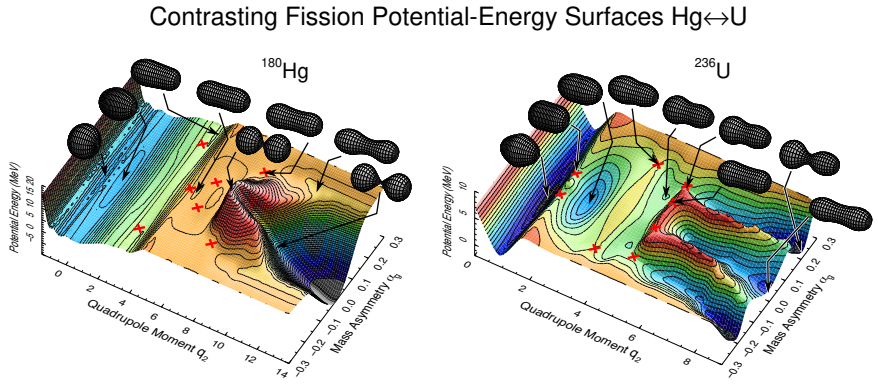

Fig. 18 (Color online). Calculated PES surfaces for ^{180}Hg and ^{236}U, as a function of the dimensionless quadrupole moment and the mass asymmetry, as defined in Fig. 11. The shapes of the nuclei at several key deformations are drawn, connected to the points on the surface by arrows. The saddle points are indicated with red crosses. The plots are modified from [143].

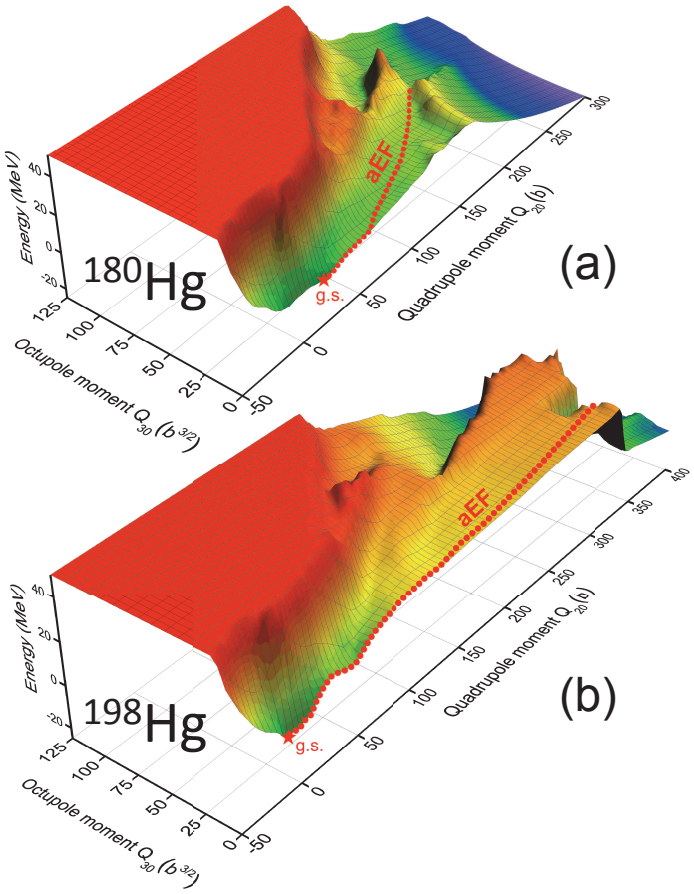

Fig. 19 (Color online) Ground-state potential-energy surfaces for (a) ^{180}Hg and (b) ^{198}Hg in the (Q_{20},Q_{30}) plane calculated in HFB-SkM*. The Q_{20} value represents the elongation along the axial symmetry, while Q_{30} parameter defines the deviation from the axial symmetry. The static fission pathway aEF corresponding to asymmetric elongated fragments is marked. The difference between the two nuclei is mainly seen in the magnitude of the final fission fragments mass asymmetry, corresponding to very different Q_{30} values. The figure is taken from [150].

3.5.3 Multimodal fission in the transitional neutron-deficient region above Z =82

Following the discovery of asymmetric fission of ^{178,180}Hg, further theoretical efforts were undertaken to cover a broader region of fission in the vicinity of the Z =82 shell closure. Extensive calculations of the mass yields for 987 nuclides were performed in Ref. [152]. The Brownian shape-motion method [153] was applied, which involves the "random walks" to determine the most probable fission path on the previously calculated five-dimensional potential-energy

surfaces [151]. One of the aims of this study was to establish theoretically whether ^{178,180}Hg represent separate cases of asymmetric fission in this region, or whether they belong to a broad contiguous region of asymmetric fission, and if so, its extent. Fig. 20 shows the map of expected asymmetric and symmetric fission, whereby a broad island of asymmetric fission in the neutron-deficient lead region is predicted. In agreement with the experimental data, this new region of asymmetric fission also includes ^{178,180}Hg, though they are predicted to lie on its left-most border. Furthermore, this island is separated from the classical region of asymmetric fission in the actinides by an extended area of symmetric fission (see the large blue region in figure).

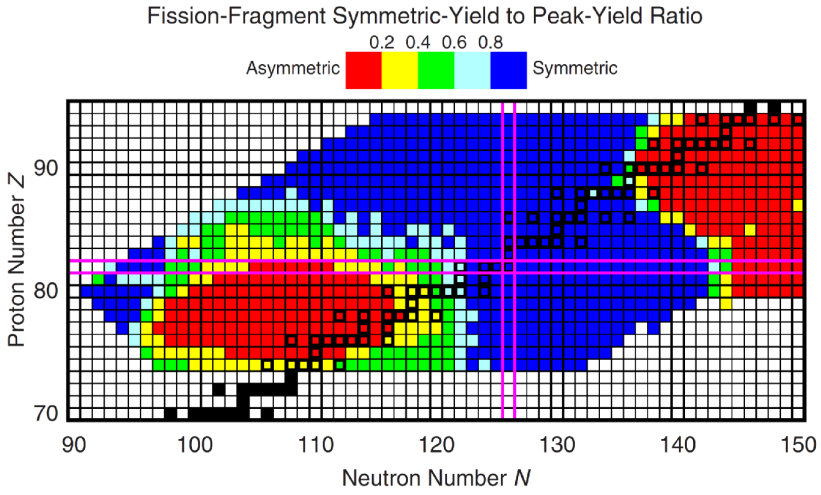

Fig. 20 (Color online) Calculated ratios of the intensities of symmetric to asymmetric fission modes for 987 fissioning isotopes. Black squares (open in colored regions, filled outside) indicate β-stable nuclei. Two extended regions of predominantly asymmetric fission (small symmetry-to-asymmetry ratios) are drawn in the red color, the one in the left bottom corner is the region of a new type of asymmetric fission and includes ^{178,180}Hg, while the previously known asymmetric fission region in the heavy actinides is seen in the top right corner. The region of predominantly symmetric fission in between is shown in blue. The figure is taken from [152].

Therefore, to explore further this region, and especially the predicted asymmetric-to-symmetric transition of FFMDs between ^{178,180}Hg and e.g. ^{204,208}Rn,^{210}Ra (which are known to fission symmetrically), the βDF experiments at ISOLDE aimed at studies of transitional βDF isotopes of ^{194,196}At and ^{202}Fr [131,116]. The low-energy fission data for daughter (after β decay) isotopes ^{194,196}Po

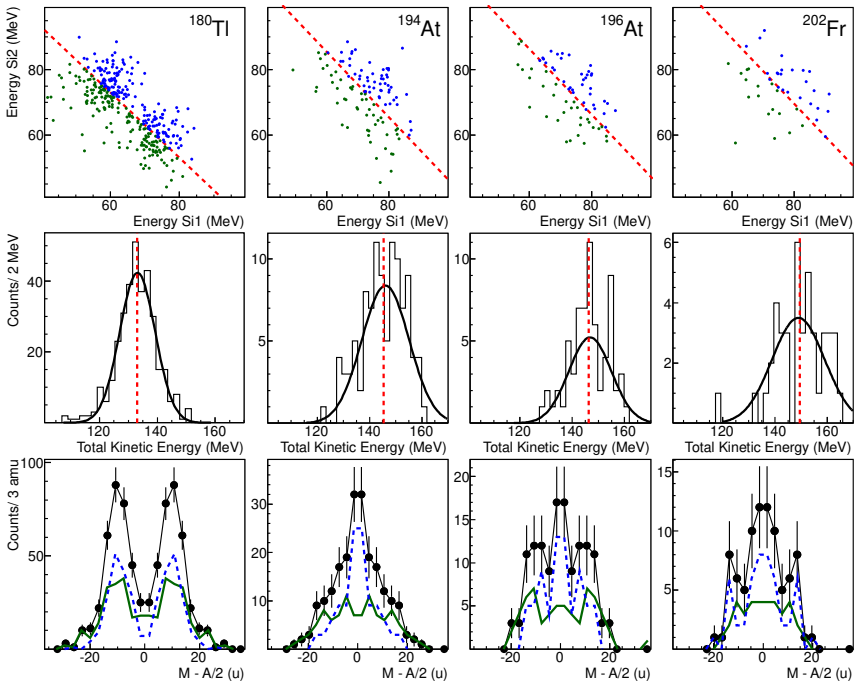

Fig. 21 (Color online) Summary plot of the ISOLDE experiments to study βDF of ^{180}Tl, ^{194,196}At and ^{202}Fr. 2D energy distribution of coincident fission fragments in two silicon detectors (top), total kinetic energy (middle) and mass distributions (bottom) of the investigated nuclei are shown. The green and blue curves represent data below and above the average TKE values for each case shown by the red dashed lines in the first and second rows of the plot. Details are given in the main text. Figure is taken from [131,116].

and ^{202}Rn, respectively, were collected. A summary of the results is shown in Fig. 21.

Experimentally, the mixture of two fission modes can be directly manifested by the two observables: the appearance of 3 peaks in the fission fragments energy distribution and by the skewness/broadness of the TKE distribution for fission fragments.

To illustrate these effects, for a reference, the top panel in the leftmost column of Fig. 21 shows the two-dimensional Si1-Si2 energy plot of coincident FFs of the daughter isotope ^{180}Hg (the same plot as in Fig. 17). The dominant asymmetric fission of ^{180}Hg is clearly demonstrated by a double-humped structure seen in this plot, with practically no events in between the peaks. The respective single-peaked and quite narrow Gaussian-like TKE distribution, depicted in the middle panel of the same column, indicates that a single fission mode dominates in ^{180}Hg. Finally, the deduced clearly asymmetric FFMD is depicted in black in the bottom panel, whereby the most probable fission fragments were found in the vicinity of ^{80}Kr and ^{100}Ru.

The results for βDF studies of ^{194,196}At and ^{202}Fr are shown in the second-to-fourth columns in Fig 21. In contrast to ^{180}Hg, a single broad hump is seen in the 2D energy distribution of ^{194,196}Po and ^{202}Rn (top row, columns 2-4). In addition, TKE distributions are significantly broader compared to the ^{180}Hg reference (middle row), as can be concluded from the standard deviation values, extracted from single-Gaussian fits, see [131] for details. Deduced FFMDs spectra, drawn in black in the bottom row, exhibit a mixture of symmetry with asymmetry, resulting in their triple-humped shape.

The triple-humped FFMDs and the breadth of the extracted TKE distributions suggest the presence of at least two distinct fission modes in these nuclei, each having different mass and TKE distributions. This feature was therefore further investigated by discriminating between fission events with high or low TKE, similar to the method used in Refs. [154,155] to illustrate the bimodal fission in the transfermium region. In Fig. 21, FFMDs of fission events with respectively higher or lower TKE in comparison to a certain threshold energy $E_{\rm thres}$ are shown by respectively the dashed blue and full green lines. The value $E_{\rm thres}$ was arbitrarily taken as the mean TKE value and is indicated by a dashed red line on the TKE distributions and the 2D energy plots. Remarkably, the ^{194,196}Po cases exhibit a narrow symmetric distribution for fragments with higher TKE, while a broader, possibly asymmetric structure is observed for lower TKE. In contrast, this feature is absent in ^{180}Hg in which only one asymmetric fission mode was identified. In the case of ^{202}Rn, statistics prohibit drawing definitive conclusions.

These results establish a multimodal fission for these three isotopes, lying in the transitional region between the asymmetry of ^{178,180}Hg and symmetry of e.g. ^{204,208}Rn and ^{210}Ra. Self-consistent PES calculations performed within the HBF-D1S framework [150] provide a clear insight in the underlying reasons for the occurrence of the multimodal fission in this region. As an example, Fig. 22 shows the PES for ^{196}Po, where two distinct competing paths - an asymmetric and symmetric - are marked. Beyond $Q_{20} = 250$ b, the PES flattens in such a way that a mildly asymmetric fission pathway competes with the symmetric pathway, which allows multimode fission to happen.

Such a flat, relatively structure-less PES is expected to represent quite a general behavior of PES's in this region of nuclei, and it is very different from the typical PES's in the actinides, where a dominant asymmetric valley is usually present, as discussed in respect of Fig. 18. It is also very different from the PES's for e.g. ^{180}Hg, which might indicate that the fission below and above the shell closure at Z=82 also has some inherent differences. Clearly, the outcome of any FFMD calculations on such flat PES's will strongly depend on specific details of a subtle and complex interplay between several degrees of freedom, including a yet not fully understood dependence on the excitation energy. In such a way, these data provide a crucial text of the modern fission approaches.

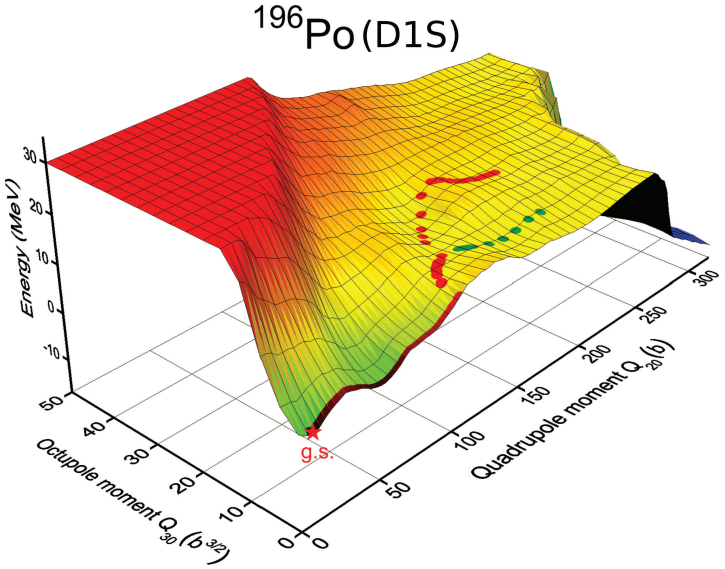

Fig. 22 (Color online) Ground-state PES for ^{196}Po in the (Q_{20},Q_{30}) plane calculated in the HFB-D1S approach. Two competing fission pathways corresponding to different mass asymmetries are marked. The figure is taken from [150].

3.5.4 Complementary approaches to study low-energy fission in the lead region

Unfortunately, due to relatively low fission rates of only up to some tens fissions per hour in the present βDF experiments at ISOLDE, no further details could be extracted, unless much longer experiments are performed. In this respect, earlier and recent experiments exploiting the Coulomb excitation of relativistic radioactive beam followed by fission at the SOFIA setup at GSI [156], have all potential to establish a complementary way for low-energy fission studies in this region. One of the main advantages of SOFIA is its access to all types of nuclides - odd-odd, even-even and odd-A, while only the odd-odd cases can be studied via βDF, see Section 3.2. The feasibility of this approach was already confirmed by the first SOFIA campaign, which reached some of the neutron-deficient Hg isotopes.

This complementarity is demonstrated by Fig. 23, which shows a subset of the calculated data from Fig. 20, but in the mass-yield representation, with selected examples (solely due to the space limitation) of the measured FFMDs via βDF, Coulex and fusion-fission approaches. A good agreement between measured and calculated FFMDs can be noted for many nuclides, shown in the plot, e.g. for ^{180}Hg, ^{201}Tl, ^{210}Po, ^{204,208}Rn, ^{210}Ra. On the other hand, one also notices a clear discrepancy for e.g. ^{195}Au and ^{198}Hg, for which a strongly asymmetric mass division is predicted, while experimentally a symmetric mass split was observed, see also [131] for further details.

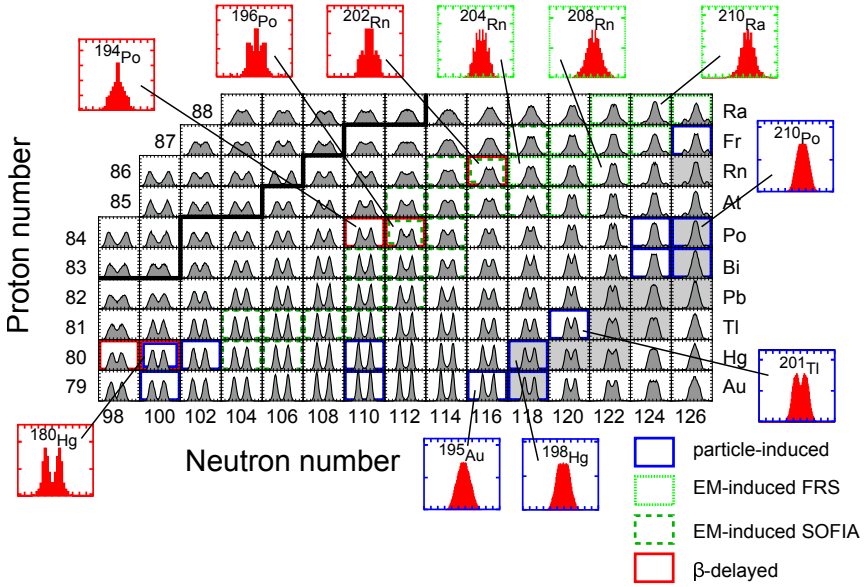

Fig. 23 (Color online) Calculated FFMDs (gray), with fission-fragment masses on the horizontal and their relative yields on the vertical axis, for even-N neutron-deficient isotopes between gold and radium at excitation energies slightly above the theoretical fission-barrier heights $B_{\mathrm{f,th}}$ from Ref. [114]. The calculated yields are compared with selected experimental FFMDs from particle-induced (blue symbols, [157,158]), βDF (red, [129,120,131]) and Coulex-induced fission from FRS@GSI (green, [98,99]) and SOFIA (dashed light green, [156]. The isotopes ^{180,190}Hg [159], ^{182}Hg [160] and ^{179,189}Au [161], recently measured by fusion-fission reactions are also marked in blue. The border of the lightest known isotopes is shown by the thick solid line, β-stable nuclei are shown on a gray background. Figure is modified from [131].

3.6 β-delayed fission rates and their use to determine fission barrier heights

The previous sections concentrated mainly on the fission fragments energy/mass distributions and their theoretical interpretation. In this section, we will discuss what interesting physics conclusions can be drawn from the measured βDF probabilities.

At present, it is believed that βDF could, together with neutron-induced and spontaneous fission, influence the fission-recycling in r-process nucleosynthesis [93,94]. Therefore, a reliable prediction of the relative importance of βDF in nuclear decay, often expressed by the βDF probability $P_{\beta\mathrm{DF}}$, is needed. $P_{\beta\mathrm{DF}}$ is defined as

$$P_{\beta\mathrm{DF}} = \frac{N_{\beta\mathrm{DF}}}{N_{\beta}}, \tag{22}$$

where $N_{\beta DF}$ and N_{β} are respectively the number of βDF and β decays of the precursor nucleus.

Before the recent βDF experiments in the lead region, a comparison of $P_{\beta\mathrm{DF}}$ data in a relatively narrow region of nuclei in the vicinity of uranium

showed a simple exponential dependence with respect to Q_β [136,162]. These nuclei have comparable and relative low $Q_\beta(Parent)$ and fission-barrier heights $B_\mathrm{f}(Daughter)$ values, $Q_\beta \sim 3-6\,\mathrm{MeV}$ and $B_\mathrm{f} \sim 4-6\,\mathrm{MeV}$, respectively. In addition, these nuclei have a typical N/Z ratio around $\sim 1.4-1.5$, which is close to that of traditional spontaneous fission of heavy actinides.

The recent βDF studies at ISOLDE allow to further explore such systematic features by including the newly obtained data in the neutron-deficient lead region, in which the βDF nuclides have significantly different N/Z ratios ($\sim 1.2-1.3$), B_f ($\sim 7-10\,\mathrm{MeV}$) and Q_β values ($\sim 9-11\,\mathrm{MeV}$) as compared to those in the uranium region.
However, from an experimental point of view, the dominant α-branching ratio ($\geq 90\,\%$) in most βDF precursors in the neutron-deficient lead region [17] makes precise determination of N_β in equation (22) difficult. Therefore, the partial βDF half-life $T_{1/2,\beta\mathrm{DF}}$, as discussed in details in [110], can be useful.

By analogy with other decay modes, $T_{1/2,\beta\mathrm{DF}}$ is defined by

$$T_{1/2,\beta\mathrm{DF}} = T_{1/2}\frac{N_\mathrm{dec,tot}}{N_{\beta\mathrm{DF}}}, \tag{23}$$

where $T_{1/2}$ represents the total half-life and $N_\mathrm{dec,tot}$ the number of decayed precursor nuclei. The relation between $T_{1/2,\beta\mathrm{DF}}$ and $P_{\beta\mathrm{DF}}$ can be derived from equations (22) and (23) as

$$T_{1/2,\beta\mathrm{DF}} = \frac{T_{1/2}}{b_\beta P_{\beta\mathrm{DF}}}, \tag{24}$$

with b_β denoting the β-branching ratio. If the α-decay channel dominates, as is often the case in the neutron-deficient lead region, one can safely approximate $N_\mathrm{dec,tot}$ in equation (23) by the amount of α decays N_α. This removes part of the systematic uncertainties as the fission fragments and the alpha decay are detected in the same silicon detector with identical detection efficiency.

Following [163,132], the expression for $P_{\beta\mathrm{DF}}$, as a function of excitation energy E, is given by

$$P_{\beta\mathrm{DF}} = \frac{\int_0^{Q_\beta} S_\beta(E)F(Q_\beta - E)\frac{\Gamma_\mathrm{f}(E)}{\Gamma_\mathrm{tot}(E)}dE}{\int_0^{Q_\beta} S_\beta(E)F(Q_\beta - E)dE}, \tag{25}$$

whereby the β-strength function of the parent nucleus is denoted by S_β and the Fermi function by F. The fission and total decay widths of the daughter, after β decay, are respectively given by Γ_f and Γ_tot. Equation (24) can be combined with equation (25) to deduce the decay constant of βDF, defined as $\lambda_{\beta\mathrm{DF}} = \ln(2)/T_{1/2,\beta\mathrm{DF}}$, as

$$\lambda_{\beta\mathrm{DF}} = \int_0^{Q_\beta} S_\beta(E)F(Q_\beta - E)\frac{\Gamma_\mathrm{f}(E)}{\Gamma_\mathrm{tot}(E)}dE. \tag{26}$$

This expression shows a few important points. First of all, the strong dependence on the fission barrier B_f of the daughter nucleus (via the Γ_f) allows

the determination of its fission barrier. This method was indeed used in several studies, see e.g. [122,124,164,125]. It is important to note that, by exploring four variants of β strength function, it was suggested that a specific choice of S_β only weakly influences the calculation of $P_{\beta\mathrm{DF}}$ [125]. The Fermi function F can be fairly well described by a function linearly proportional to $(Q_{EC}-E)^2$ [110] for EC decay.

A dedicated study [110] was performed to verify the Eq. 26 by using experimental βDF partial half-lives and theoretical values for $(Q_\beta - B_\mathrm{f})$. Tabulated fission barriers from four different fission models were used (see Table 1 in [110]), of which three are based on a macroscopic-microscopic and one on a mean-field approach. The latter model employs the Extended Thomas-Fermi plus Strutinsky Integral (ETFSI) method [165], but tabulated barriers for the most neutron-deficient isotopes of our interest are absent in literature. The microscopic-macroscopic approaches all rely on shell corrections from [113] and describe the macroscopic structure of the nucleus by either a TF model [115], LDM [166] or the FRLDM [114]. The Q_β values were taken from the 2012 atomic mass evaluation tables [17] and are derived from the difference between the atomic masses of parent M_P and daughter M_D nuclei.

Figure 24 shows $\log_{10}(T_{1/2,\beta\mathrm{DF}})$ against $(Q_\beta - B_\mathrm{f})$ for the fission barriers from the four different models under consideration. Using the same evaluation criteria as proposed in [105] for $P_{\beta\mathrm{DF}}$ measurements, 13 reliable $T_{1/2,\beta\mathrm{DF}}$ values, were selected. These data points, represented by the closed symbols, are fitted by a linear function. An equal weight to all fit points is given because the experimental uncertainties on $\log_{10}(T_{1/2,\beta\mathrm{DF}})$ are in most cases much smaller than the deviation of the data points with the fitted line. The remaining data points from Table 1 from [110] are shown by open symbols and were excluded from the fit. The color code discriminates between the neutron-deficient lead region (red), neutron-deficient (black) and neutron-rich (blue) uranium region.

Figure 24 illustrates a linear dependence of $\log_{10}(T_{1/2,\beta\mathrm{DF}})$ on $(Q_\beta - B_\mathrm{f})$ for TF and LDM barriers for over 7 orders of magnitude of $T_{1/2,\beta\mathrm{DF}}$. The dependence is somewhat less pronounced for the FRLDM model. A similar linear trend is observed for the ETFSI model, but the lack of tabulated fission barriers in the neutron-deficient region, especially in the lead region, prohibits drawing definite conclusions.

In contrast to a rather good agreement for most neutron-deficient nuclei, all models show a larger systematical deviation from this linear trend for the neutron-rich βDF precursors ^{228}Ac and ^{234,236}Pa. In [105], concerns were raised on the accuracy of the $P_{\beta\mathrm{DF}}$ values measured in this region, which could explain this deviation. Note also that the precursors in this region of the nuclear chart undergo β^- decay in contrast to the EC-delayed fission on the neutron-deficient side for which equation (26) was deduced. In particular, the Fermi function for β^- decay is approximately proportional to $(Q_\beta - E)^5$ [167,132], in contrast to the quadratic dependence on $(Q_\beta - E)$ for EC decay, and some modifications of the $\Gamma_\mathrm{f}/\Gamma_\mathrm{tot}$ ratio might need to be considered, see [110].

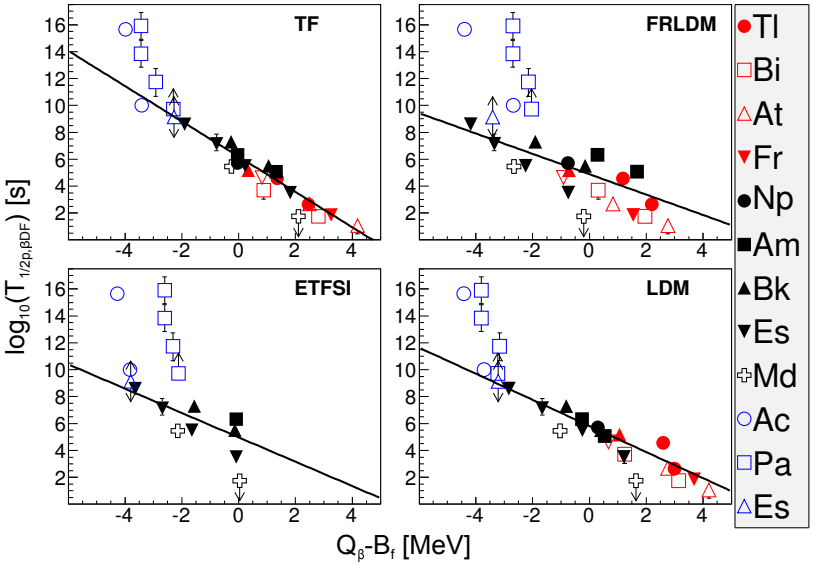

Fig. 24 (Color online) Plots of $T_{1/2,\beta\mathrm{DF}}$ versus $(Q_\beta - B_\mathrm{f})$ for four different models, see the main text. The closed symbols, representing "reliable" values for $T_{1/2,\beta\mathrm{DF}}$ are used for a linear fit with equal weights to the data points. Other data are indicated by the open symbols. The color code represents the different regions of the nuclear chart for which βDF has been experimentally observed : the neutron-deficient lead region (red), the neutron-deficient (black) and neutron-rich (blue) uranium region.

4 Conclusion and outlook

Despite α decay was discovered more then a century ago and fission almost 80 years ago, a full microscopic understanding of these important decay processes is still missing.

α decay is now a standard experimental tool in radioactive beam research programs. As an example, we discussed its use to unravel nuclear-structure effects in the $N \sim Z$ nuclei in the vicinity of ^{100}Sn and the neutron-deficient lead region. α decay is furthermore indispensable for the study and identification of new elements and new superheavy isotopes. While not explicitly addressed in these notes, it plays an important role in the atomic physics and chemistry research program at the end of Mendeleev's table.

βDF represents a unique probe to study low-energy fission and provides new information that improves our understanding of fission. With the availability of intense neutron-deficient beams in the lead region and using the mechanism of βDF, the low-energy fission process could be characterized in a new area of the nuclear chart previously unexplored by low-energy fission. A new region of asymmetric fission was identified and this finding had an impact on the theoretical description of the fission process.

New or upgraded facilities that will become operational in the next decade will have a profound impact on this research field. Facilities like e.g. the Dubna

superheavy element factory, the GARIS2 separators at RIKEN, the new heavy ion injector at GSI and the Super Separator Spectrometer (S3) at GANIL, will use higher primary beam intensities and longer beam times. This creates potential to discover new elements and isotopes but it will, at the same time, allow for more detailed and higher precision studies in the heavy and superheavy element region. Also the plans to develop the next generation ISOL facility, called the European Isotope Separator On-Line (EURISOL) facility, will have major impact on α and βDF studies in the heavy element region both on the neutron-deficient and neutron-rich side. For example, provided the necessary degree of isomer selectivity can be reached, βDF studies on isomeric beams might become possible. Moreover, new observables, like prompt neutron and γ-ray energies and multiplicities, will become available as well as more accurate fission fragment yield distributions, total kinetic energies and βDF probabilities for very neutron-rich nuclei. This information will guide refinements and improvements of the nuclear models used to explain e.g. the r-process nucleosynthesis.

Finally, it should be mentioned that α decay and fission are important in practical applications like medical radioisotope and energy production. An in-depth understanding of both processes might also lead to more efficient procedures and new usage in the applied sector.

Acknowledgements PVD acknowledges the support from KU Leuven Research Office, the Research Foundation - Flanders (FWO Vlaanderen) and the IAP network program P8/12 (Belgian Science Policy office). AA acknowledges the support from Science and Technology Facilities Council of the UK.

References

1. Huyse, M. *The Why and How of Radioactive-Beam Research, in: Lecture Notes in Physics*, volume 651, 1–32. Springer Berlin Heidelberg (2004).
2. Gamow, G. *Zeitschrift für Physik A Hadrons and Nuclei* **51**, 204–212 (1928). 10.1007/BF01343196.
3. Gurney, R. and Condon, E. *Nature* **122**, 439 (1928).
4. Gurney, R. W. and Condon, E. U. *Phys. Rev.* **33**, 127–140 Feb (1929).
5. Hahn, O. and Strassmann, F. *Naturwissenschaften* **27**, 11–15 (1939).
6. Bohr, N. and Wheeler, J. A. *Phys. Rev.* **56**, 426–450 Sep (1939).
7. Angulo, C. *Experimental Tools for Nuclear Astrophysics, in: Lecture Notes in Physics*, volume 761, 253–282. Springer Berlin Heidelberg (2009).
8. Langanke, K., Thielemann, F.-K., and Wiescher, M. *Nuclear Astrophysics and Nuclei Far from Stability, in: Lecture Notes in Physics*, volume 651, 383–467. Springer Berlin Heidelberg (2004).
9. Van Duppen, P. *Isotope Separation On Line and Post Acceleration, in: Lecture Notes in Physics on Physics*, volume 700, 37–77. Springer Berlin Heidelberg (2006).
10. Heyde, K. *Basic Ideas and Concepts in Nuclear Physics: an Introductory Approach, Institute of Physics, Series in Fundamental and Applied Nuclear Physics - 3^{th} edition, Institute of Physics Publishing, Bristol and Philadelphia* (2004).
11. Wong, S. S. M. *Introductory Nuclear Physics, John Wiley & Sons* (1998).
12. Loveland, W. D., Morrissey, D. J., and Seaborg, G. T. *Modern Nuclear Chemistry, John Wiley & Sons* (2006).
13. Roeckl, E. *Alpha Decay, in: Nuclear Decay Modes*, 237–274. IOP Publishing, Bristol and Philadelphia (1996).

14. Roeckl, E. *Decay Studies of N/Z Nuclei, in: Lecture Notes in Physics*, volume 651, 223–261. Springer Berlin Heidelberg (2004).
15. Delion, D. S. *Theory of Particle and Cluster Emission, in: Lecture Notes in Physics*, volume 819, 3 – 293. Springer Berlin Heidelberg (2010).
16. Audi, G., Wang, M., Wapstra, A., Kondev, F., MacCormick, M., Xu, X., and Pfeiffer, B. *Chinese Phys. C* **36**, 1287 (2012).
17. Wang, M., Audi, G., Wapstra, A. H., Kondev, F. G., MacCormick, M., Xu, X., and Pfeiffer, B. *Chinese Physics C* , 1287–2014 (2012).
18. de Marcillac, P., Coron, N., Dambier, G., Leblanc, J., and Moalic, J.-P. *Nature* **422**(6934), 876–878 Apr (2003).
19. Geiger, H. and Nuttall, J. *Philosophical Magazine* **22**(130), 613–621 (1911).
20. Geiger, H. *Zeitschrift für Physik* **8**(1), 45–57 (1922).
21. Viola, V. and Seaborg, G. *Journal of Inorganic and Nuclear Chemistry* **28**(3), 741 – 761 (1966).
22. Brown, B. A. *Phys. Rev. C* **46**, 811–814 Aug (1992).
23. Koura, H. *Journal of Nuclear Science and Technology* **49**(8), 816–823 (2012).
24. Ni, D. and Ren, Z. *Annals of Physics* **358**, 108 – 128 (2015). School of Physics at Nanjing University.
25. Qi, C., Andreyev, A., Huyse, M., Liotta, R., Duppen, P. V., and Wyss, R. *Physics Letters B* **734**, 203 – 206 (2014).
26. Buck, B., Merchant, A. C., and Perez, S. M. *Phys. Rev. Lett.* **65**, 2975–2977 Dec (1990).
27. Buck, B., Merchant, A., and Perez, S. *Atomic Data and Nuclear Data Tables* **54**(1), 53 – 73 (1993).
28. Buck, B., Merchant, A. C., and Perez, S. M. *Phys. Rev. C* **45**, 2247–2253 May (1992).
29. Andreyev, A. N., Huyse, M., Van Duppen, P., Qi, C., Liotta, R. J., Antalic, S., Ackermann, D., Franchoo, S., Heßberger, F. P., Hofmann, S., Kojouharov, I., Kindler, B., Kuusiniemi, P., Lesher, S. R., Lommel, B., Mann, R., Nishio, K., Page, R. D., Streicher, B., Šáro, i. c. v., Sulignano, B., Wiseman, D., and Wyss, R. A. *Phys. Rev. Lett.* **110**, 242502 Jun (2013).
30. Rasmussen, J. O. *Phys. Rev.* **113**, 1593–1598 Mar (1959).
31. Qi, C., Xu, F. R., Liotta, R. J., and Wyss, R. *Phys. Rev. Lett.* **103**, 072501 Aug (2009).
32. Qi, C., Xu, F. R., Liotta, R. J., Wyss, R., Zhang, M. Y., Asawatangtrakuldee, C., and Hu, D. *Phys. Rev. C* **80**, 044326 Oct (2009).
33. Lovas, R., Liotta, R., Insolia, A., Varga, K., and Delion, D. *Physics Reports* **294**(5), 265 – 362 (1998).
34. Wauters, J., Dendooven, P., Huyse, M., Reusen, G., Van Duppen, P., and Lievens, P. *Phys. Rev. C* **47**, 1447–1454 Apr (1993).
35. Mang, H. J. *Phys. Rev.* **119**, 1069–1075 Aug (1960).
36. Fliessbach, T., Mang, H. J., and Rasmussen, J. O. *Phys. Rev. C* **13**, 1318–1323 Mar (1976).
37. Thomas, R. G. *Progress of Theoretical Physics* **12**(3), 253 (1954).
38. Varga, K., Lovas, R. G., and Liotta, R. J. *Phys. Rev. Lett.* **69**, 37–40 Jul (1992).
39. Qi, C., Andreyev, A. N., Huyse, M., Liotta, R. J., Van Duppen, P., and Wyss, R. A. *Phys. Rev. C* **81**, 064319 Jun (2010).
40. Delion, D. S., Insolia, A., and Liotta, R. J. *Phys. Rev. C* **46**, 1346–1354 Oct (1992).
41. Delion, D. S., Peltonen, S., and Suhonen, J. *Phys. Rev. C* **73**, 014315 Jan (2006).
42. Patial, M., Liotta, R. J., and Wyss, R. *Phys. Rev. C* **93**, 054326 May (2016).
43. Liddick, S. N., Grzywacz, R., Mazzocchi, C., Page, R. D., Rykaczewski, K. P., Batchelder, J. C., Bingham, C. R., Darby, I. G., Drafta, G., Goodin, C., Gross, C. J., Hamilton, J. H., Hecht, A. A., Hwang, J. K., Ilyushkin, S., Joss, D. T., Korgul, A., Królas, W., Lagergren, K., Li, K., Tantawy, M. N., Thomson, J., and Winger, J. A. *Phys. Rev. Lett.* **97**, 082501 Aug (2006).
44. Darby, I. G., Grzywacz, R. K., Batchelder, J. C., Bingham, C. R., Cartegni, L., Gross, C. J., Hjorth-Jensen, M., Joss, D. T., Liddick, S. N., Nazarewicz, W., Padgett, S., Page, R. D., Papenbrock, T., Rajabali, M. M., Rotureau, J., and Rykaczewski, K. P. *Phys. Rev. Lett.* **105**, 162502 Oct (2010).

45. Poenaru, D. N., Ivascu, M., and Sandulescu, A. *Journal of Physics G: Nuclear Physics* **5**(10), L169 (1979).
46. Poenaru, D. N. and Greiner, W. *Fission approach to alpha-decay in superheavy nuclei*, 321–328. World Scientific (2012).
47. Düllmann, C. E. *Nuclear Instruments and Methods in Physics Research Section B: Beam Interactions with Materials and Atoms* **266**(19), 4123 – 4130 (2008). Proceedings of the XVth International Conference on Electromagnetic Isotope Separators and Techniques Related to their Applications.
48. Borge, M. and Blaum, K. *J. Phys. G: Nucl. Part. Phys.* **44** (2017).
49. Dilling, J., Krücken, R., and Merminga, L. *Hyperfine Interactions* **225**, 1–282 (2014).
50. Liu, Z., Kurcewicz, J., Woods, P., Mazzocchi, C., Attallah, F., Badura, E., Davids, C., Davinson, T., Dring, J., Geissel, H., Grska, M., Grzywacz, R., Hellstrm, M., Janas, Z., Karny, M., Korgul, A., Mukha, I., Pftzner, M., Plettner, C., Robinson, A., Roeckl, E., Rykaczewski, K., Schmidt, K., Seweryniak, D., and Weick, H. *Nuclear Instruments and Methods in Physics Research Section A: Accelerators, Spectrometers, Detectors and Associated Equipment* **543**(2), 591 – 601 (2005).
51. Kurcewicz, J., Liu, Z., Pftzner, M., Woods, P., Mazzocchi, C., Schmidt, K.-H., Keli, A., Attallah, F., Badura, E., Davids, C., Davinson, T., Dring, J., Geissel, H., Grska, M., Grzywacz, R., Hellstrm, M., Janas, Z., Karny, M., Korgul, A., Mukha, I., Plettner, C., Robinson, A., Roeckl, E., Rykaczewski, K., Schmidt, K., Seweryniak, D., Smmerer, K., and Weick, H. *Nuclear Physics A* **767**, 1 – 12 (2006).
52. Morrissey, D. J. and Sherrill, B. M. *In-Flight Separation of Projectile Fragments, in: Lecture Notes in Physics*, volume 651, 113–135. Springer Berlin Heidelberg (2004).
53. Hofmann, S. *Journal of Physics G: Nuclear and Particle Physics* **42**(11), 114001 (2015).
54. Andreyev, A. N., Ackermann, D., Heßberger, F. P., Hofmann, S., Huyse, M., Münzenberg, G., Page, R. D., Van de Vel, K., and Van Duppen, P. *Nucl. Instrum. Methods A* **533**(3), 409 – 421 (2004).
55. Andreyev, A. N., Antalic, S., Huyse, M., Van Duppen, P., Ackermann, D., Bianco, L., Cullen, D. M., Darby, I. G., Franchoo, S., Heinz, S., Heßberger, F. P., Hofmann, S., Kojouharov, I., Kindler, B., Leppänen, A. P., Lommel, B., Mann, R., Münzenberg, G., Pakarinen, J., Page, R. D., Ressler, J. J., Saro, S., Streicher, B., Sulignano, B., Thomson, J., and Wyss, R. *Phys. Rev. C* **74**, 064303 Dec (2006).
56. Münzenberg, G., Faust, W., Hofmann, S., Armbruster, P. Güttner, K., and Ewald, H. *Nuclear Instruments and Methods* **161**(1), 65 – 82 (1979).
57. Hofmann, S. *Superheavy Elements, in: Lecture Notes in Physics*, volume 761, 203–252. Springer Berlin Heidelberg (2009).
58. Oganessian, Y. T. and Utyonkov, V. K. *Reports on Progress in Physics* **78**(3), 036301 (2015).
59. Janas, Z., Mazzocchi, C., Batist, L., Blazhev, A., Górska, M., Kavatsyuk, M., Kavatsyuk, O., Kirchner, R., Korgul, A., La Commara, M., Miernik, K., Mukha, I., Płochocki, A., Roeckl, E., and Schmidt, K. *The European Physical Journal A - Hadrons and Nuclei* **23**(2), 197–200 (2005).
60. Seweryniak, D., Carpenter, M. P., Gros, S., Hecht, A. A., Hoteling, N., Janssens, R. V. F., Khoo, T. L., Lauritsen, T., Lister, C. J., Lotay, G., Peterson, D., Robinson, A. P., Walters, W. B., Wang, X., Woods, P. J., and Zhu, S. *Phys. Rev. Lett.* **99**, 022504 Jul (2007).
61. Neugart, R. and Neyens, G. *Nuclear Moments, in: Lecture Notes in Physics*, volume 700, 135–189. Springer Berlin Heidelberg (2006).
62. Ferrer, R., Barzakh, A., Bastin, B., Beerwerth, R., Block, M., Creemers, P., Grawe, H., de Groote, R., Delahaye, P., Fléchard, X., Franchoo, S., Fritzsche, S., Gaffney, L. P., Ghys, L., Gins, W., Granados, C., Heinke, R., Hijazi, L., Huyse, M., Kron, T., Kudryavtsev, Y., Laatiaoui, M., Lecesne, N., Loiselet, M., Lutton, F., Moore, I. D., Martínez, Y., Mogilevskiy, E., Naubereit, P., Piot, J., Raeder, S., Rothe, S., Savajols, H., Sels, S., Sonnenschein, V., Thomas, J.-C., Traykov, E., Van Beveren, C., Van den Bergh, P., Van Duppen, P., Wendt, K., and Zadvornaya, A. *Nature Communications* **8**, 14520 Feb (2017).
63. Morinaga, H. *Phys. Rev.* **101**, 254–258 Jan (1956).

64. Heyde, K. and Wood, J. L. *Rev. Mod. Phys.* **83**, 1467–1521 Nov (2011).
65. Wood, J. L. and Heyde, K. *Journal of Physics G: Nuclear and Particle Physics* **43**(2), 020402 (2016).
66. Elseviers, J., Andreyev, A. N., Antalic, S., Barzakh, A., Bree, N., Cocolios, T. E., Comas, V. F., Diriken, J., Fedorov, D., Fedosseyev, V. N., Franchoo, S., Heredia, J. A., Huyse, M., Ivanov, O., Köster, U., Marsh, B. A., Page, R. D., Patronis, N., Seliverstov, M., Tsekhanovich, I., Van den Bergh, P., Van De Walle, J., Van Duppen, P., Venhart, M., Vermote, S., Veselský, M., and Wagemans, C. *Phys. Rev. C* **84**, 034307 Sep (2011).
67. Andreyev, A. N., Huyse, M., Van Duppen, P., Weissman, L., Ackermann, D., Gerl, J., Heßberger, F. P., Hofmann, S., Kleinbohl, A., Munzenberg, G., Reshitko, S., Schlegel, C., Schaffner, H., Cagarda, P., Matos, M., Saro, S., Keenan, A., Moore, C., O'Leary, C. D., Page, R. D., Taylor, M., Kettunen, H., Leino, M., Lavrentiev, A., Wyss, R., and Heyde, K. *Nature* **405**(6785), 430–433 May (2000).
68. De Witte, H., Andreyev, A. N., Barré, N., Bender, M., Cocolios, T. E., Dean, S., Fedorov, D., Fedoseyev, V. N., Fraile, L. M., Franchoo, S., Hellemans, V., Heenen, P. H., Heyde, K., Huber, G., Huyse, M., Jeppessen, H., Köster, U., Kunz, P., Lesher, S. R., Marsh, B. A., Mukha, I., Roussière, B., Sauvage, J., Seliverstov, M., Stefanescu, I., Tengborn, E., Van de Vel, K., Van de Walle, J., Van Duppen, P., and Volkov, Y. *Phys. Rev. Lett.* **98**, 112502 Mar (2007).
69. Cocolios, T. E., Dexters, W., Seliverstov, M. D., Andreyev, A. N., Antalic, S., Barzakh, A. E., Bastin, B., Büscher, J., Darby, I. G., Fedorov, D. V., Fedosseyev, V. N., Flanagan, K. T., Franchoo, S., Fritzsche, S., Huber, G., Huyse, M., Keupers, M., Köster, U., Kudryavtsev, Y., Mané, E., Marsh, B. A., Molkanov, P. L., Page, R. D., Sjoedin, A. M., Stefan, I., Van de Walle, J., Van Duppen, P., Venhart, M., Zemlyanoy, S. G., Bender, M., and Heenen, P.-H. *Phys. Rev. Lett.* **106**, 052503 Feb (2011).
70. Julin, R., Grahn, T., Pakarinen, J., and Rahkila, P. *Journal of Physics G: Nuclear and Particle Physics* **43**(2), 024004 (2016).
71. Delion, D., Florescu, A., Huyse, M., Wauters, J., Van Duppen, P., Insolia, A., Liotta, R., Collaboration, I., et al. *Physical review letters* **74**(20), 3939 (1995).
72. Xu, C. and Ren, Z. *Phys. Rev. C* **75**, 044301 Apr (2007).
73. Delion, D. S., Florescu, A., Huyse, M., Wauters, J., Van Duppen, P., Insolia, A., and Liotta, R. J. *Phys. Rev. Lett.* **74**, 3939–3942 May (1995).
74. Karlgren, D., Liotta, R. J., Wyss, R., Huyse, M., Vel, K. V. d., and Duppen, P. V. *Phys. Rev. C* **73**, 064304 Jun (2006).
75. Delion, D. S., Liotta, R. J., Qi, C., and Wyss, R. *Phys. Rev. C* **90**, 061303 Dec (2014).
76. Oganessian, Y. and Rykaczewski, K. *Physics Today* **68**(8), 32 – 38 (2015).
77. Rudolph, D., Elding, L.-I., Fahlander, C., and berg, S. *EPJ Web Conf.* **131**, 00001 (2016).
78. Hofmann, Sigurd. *EPJ Web Conf.* **131**, 06001 (2016).
79. Bollen, G. *Traps for Rare Isotopes, in: Lecture Notes in Physics*, volume 651, 169–210. Springer Berlin Heidelberg (2004).
80. Block, M., Ackermann, D., Blaum, K., Droese, C., Dworschak, M., Eliseev, S., Fleckenstein, T., Haettner, E., Herfurth, F., Heßberger, F. P., Hofmann, S., Ketelaer, J., Ketter, J., Kluge, H.-J., Marx, G., Mazzocco, M., Novikov, Y. N., Plaß, W. R., Popeko, A., Rahaman, S., Rodríguez, D., Scheidenberger, C., Schweikhard, L., Thirolf, P. G., Vorobyev, G. K., and Weber, C. *Nature* **463**(7282), 785–788 Feb (2010).
81. Block, M. *EPJ Web Conf.* **131**, 05003 (2016).
82. Schury, P., Wada, M., Ito, Y., Kaji, D., Arai, F., MacCormick, M., Murray, I., Haba, H., Jeong, S., Kimura, S., Koura, H., Miyatake, H., Morimoto, K., Morita, K., Ozawa, A., Rosenbusch, M., Reponen, M., Söderström, P.-A., Takamine, A., Tanaka, T., and Wollnik, H. *Phys. Rev. C* **95**, 011305 Jan (2017).
83. Heßberger, F.-P. *EPJ Web Conf.* **131**, 02005 (2016).
84. Heenen, P.-H., Bally, B., Bender, M., and Ryssens, W. .
85. Gönnenwein, F. In *Contribution to the École Joliot Curie, 2014*, (2014).
86. Wagemans, C., editor. *The Nuclear Fission Process.* CRC Press, (1991).
87. Karpov, A. V., Kelić, A., and Schmidt, K.-H. *Journal of Physics G: Nuclear and Particle Physics* **35**(3), 035104 (2008).
88. Strutinsky, V. M. *Nuclear Physics A* **95**(2), 420 – 442 (1967).

89. Strutinsky, V. M. *Nuclear Physics A* **122**(1), 1 – 33 (1968).
90. Brack, M., Damgaard, J., Jensen, A. S., Pauli, H. C., Strutinsky, V. M., and Wong, C. Y. *Rev. Mod. Phys.* **44**, 320–405 Apr (1972).
91. Armbruster, P. *Reports on Progress in Physics* **62**, 465 – 525 (1998).
92. Wene, C. O. and Johansson, S. A. E. *Phys. Scr.* **10A**, 156–162 (1974).
93. Panov, I., Kolbe, E., Pfeiffer, B., Rauscher, T., Kratz, K.-L., and Thielemann, F.-K. *Nucl. Phys. A* **747**(24), 633 – 654 (2005).
94. Petermann, I., Langanke, K., Martínez-Pinedo, G., Panov, I., Reinhard, P. G., and Thielemann, F. K. *Eur. Phys. J. A* **48**, 1–11 (2012).
95. Goriely, S., Sida, J.-L., Lemaître, J.-F., Panebianco, S., Dubray, N., Hilaire, S., Bauswein, A., and Janka, H.-T. *Phys. Rev. Lett.* **111**, 242502 Dec (2013).
96. Borge, M. J. G. *Nuclear Instruments and Methods in Physics Research Section B: Beam Interactions with Materials and Atoms* **376**, 408 – 412 (2016). Proceedings of the XVIIth International Conference on Electromagnetic Isotope Separators and Related Topics (EMIS2015), Grand Rapids, MI, U.S.A., 11-15 May 2015.
97. Heßberger, F. P. *The European Physical Journal A* **53**(4), 75 (2017).
98. Schmidt, K.-H., Steinhäuser, S., Böckstiegel, C., Grewe, A., Heinz, A., Junghans, A., Benlliure, J., Clerc, H. G., de Jong, M., Müller, J., Pfützner, M., and Voss, B. *Nucl. Phys. A* **665**(34), 221 – 267 (2000).
99. Schmidt, K.-H., Benlliure, J., and Junghans, A. R. *Nucl. Phys. A* **693**, 169–189 (2001).
100. Blank, B. and Borge, M. J. G. *Progress in Particle and Nuclear Physics* **60**(2), 403 – 483 (2008).
101. Pfützner, M., Karny, M., Grigorenko, L. V., and Riisager, K. *Rev. Mod. Phys.* **84**, 567–619 Apr (2012).
102. Kuznetsov, V. I., Skobelev, N. K., and Flerov, G. N. *Yad. Fiz.* **4***, 279; [Sov. J. Nucl. Phys.* **4***, (1967), 202]* (1966).
103. Kuznetsov, V. I., Skobelev, N. K., and Flerov, G. N. *Yad. Fiz.* **5***, 271; [Sov. J. Nucl. Phys.* **5***, (1967), 191]* (1967).
104. Skobelev, N. K. *Yad. Fiz.* **15***, 444; [Sov. J. Nucl. Phys.* **15***, 249 (1972)]* (1972).
105. Andreyev, A. N., Huyse, M., and Van Duppen, P. *Rev. Mod. Phys.* **85**, 1541–1559 Oct (2013).
106. Hall, H. L., Gregorich, K. E., Henderson, R. A., Gannett, C. M., Chadwick, R. B., Leyba, J. D., Czerwinski, K. R., Kadkhodayan, B., Kreek, S. A., Lee, D. M., Nurmia, M. J., and Hoffman, D. C. *Phys. Rev. Lett.* **63**, 2548–2550 Dec (1989).
107. Hall, H. L., Gregorich, K. E., Henderson, R. A., Gannett, C. M., Chadwick, R. B., Leyba, J. D., Czerwinski, K. R., Kadkhodayan, B., Kreek, S. A., Lee, D. M., Nurmia, M. J., Hoffman, D. C., Palmer, C. E. A., and Baisden, P. A. *Phys. Rev. C* **41**, 618–630 Feb (1990).
108. Hall, H. L., Gregorich, K. E., Henderson, R. A., Gannett, C. M., Chadwick, R. B., Leyba, J. D., Czerwinski, K. R., Kadkhodayan, B., Kreek, S. A., Hannink, N. J., Lee, D. M., Nurmia, M. J., Hoffman, D. C., Palmer, C. E. A., and Baisden, P. A. *Phys. Rev. C* **42**, 1480–1488 Oct (1990).
109. Kreek, S. A., Hall, H. L., Gregorich, K. E., Henderson, R. A., Leyba, J. D., Czerwinski, K. R., Kadkhodayan, B., Neu, M. P., Kacher, C. D., Hamilton, T. M., Lane, M. R., Sylwester, E. R., Türler, A., Lee, D. M., Nurmia, M. J., and Hoffman, D. C. *Phys. Rev. C* **50**, 2288–2296 Nov (1994).
110. Ghys, L., Andreyev, A. N., Antalic, S., Huyse, M., and Van Duppen, P. *Phys. Rev. C* **91**, 044314 Apr (2015).
111. Thielemann, F. K., Metzinger, J., and Klapdor, H. *Z. Phys. A* **309**, 301–317 (1983).
112. Meyer, B. S., Howard, W. M., Mathews, G. J., Takahashi, K., Möller, P., and Leander, G. A. *Phys. Rev. C* **39**, 1876–1882 May (1989).
113. Möller, P., Nix, J. R., Myers, W. D., and Swiatecki, W. J. *Atomic Data and Nuclear Data Tables* **59**(2), 185 – 381 (1995).
114. Möller, P., Sierk, A. J., Ichikawa, T., Iwamoto, A., and Mumpower, M. *Phys. Rev. C* **91**, 024310 Feb (2015).
115. Myers, W. D. and Świątecki, W. J. *Phys. Rev. C* **60**, 014606 Jun (1999).

116. Truesdale, V. L., Andreyev, A. N., Ghys, L., Huyse, M., Van Duppen, P., Sels, S., Andel, B., Antalic, S., Barzakh, A., Capponi, L., Cocolios, T. E., Derkx, X., De Witte, H., Elseviers, J., Fedorov, D. V., Fedosseev, V. N., Heßberger, F. P., Kalaninová, Z., Köster, U., Lane, J. F. W., Liberati, V., Lynch, K. M., Marsh, B. A., Mitsuoka, S., Nagame, Y., Nishio, K., Ota, S., Pauwels, D., Popescu, L., Radulov, D., Rapisarda, E., Rothe, S., Sandhu, K., Seliverstov, M. D., Sjödin, A. M., Van Beveren, C., Van den Bergh, P., and Wakabayashi, Y. *Phys. Rev. C* **94**, 034308 Sep (2016).
117. Andreyev, A. N., Antalic, S., Ackermann, D., Franchoo, S., Heßberger, F. P., Hofmann, S., Huyse, M., Kojouharov, I., Kindler, B., Kuusiniemi, P., Lesher, S. R., Lommel, B., Mann, R., Münzenberg, G., Nishio, K., Page, R. D., Ressler, J. J., Streicher, B., Saro, S., Sulignano, B., Van Duppen, P., and Wiseman, D. R. *Phys. Rev. C* **73**, 024317 Feb (2006).
118. Andreyev, A. N., Antalic, S., Ackermann, D., Bianco, L., Franchoo, S., Heinz, S., Heßberger, F. P., Hofmann, S., Huyse, M., Kojouharov, I., Kindler, B., Lommel, B., Mann, R., Nishio, K., Page, R. D., Ressler, J. J., Sapple, P., Streicher, B., Saro, S., Sulignano, B., Thomson, J., Van Duppen, P., and Venhart, M. *Phys. Rev. C* **79**, 064320 Jun (2009).
119. Andreyev, A. N., Antalic, S., Ackermann, D., Bianco, L., Franchoo, S., Heinz, S., Heßberger, F. P., Hofmann, S., Huyse, M., Kalaninová, Z., Kojouharov, I., Kindler, B., Lommel, B., Mann, R., Nishio, K., Page, R. D., Ressler, J. J., Streicher, B., Saro, S., Sulignano, B., and Van Duppen, P. *Phys. Rev. C* **87**, 014317 Jan (2013).
120. Liberati, V., Andreyev, A. N., Antalic, S., Barzakh, A., Cocolios, T. E., Elseviers, J., Fedorov, D., Fedoseeev, V. N., Huyse, M., Joss, D. T., Kalaninová, Z., Köster, U., Lane, J. F. W., Marsh, B., Mengoni, D., Molkanov, P., Nishio, K., Page, R. D., Patronis, N., Pauwels, D., Radulov, D., Seliverstov, M., Sjödin, M., Tsekhanovich, I., Van den Bergh, P., Van Duppen, P., Venhart, M., and Veselský, M. *Phys. Rev. C* **88**, 044322 Oct (2013).
121. Lane, J. F. W., Andreyev, A. N., Antalic, S., Ackermann, D., Gerl, J., Heßberger, F. P., Hofmann, S., Huyse, M., Kettunen, H., Kleinböhl, A., Kindler, B., Kojouharov, I., Leino, M., Lommel, B., Münzenberg, G., Nishio, K., Page, R. D., Šáro, i. c. v., Schaffner, H., Taylor, M. J., and Van Duppen, P. *Phys. Rev. C* **87**, 014318 Jan (2013).
122. Klapdor, H. V., Wene, C. O., Isosimov, I. N., and Naumow, Y. W. *Z. Phys. A* **292**, 249–255 (1979).
123. Habs, D., Klewe-Nebenius, H., Metag, V., Neumann, B., and Specht, H. J. *Z. Phys. A* **285**, 53–57 (1978).
124. Staudt, A., Hirsch, M., Muto, K., and Klapdor-Kleingrothaus, H. V. *Phys. Rev. Lett.* **65**, 1543 (1990).
125. Veselský, M., Andreyev, A. N., Antalic, S., Huyse, M., Möller, P., Nishio, K., Sierk, A. J., Van Duppen, P., and Venhart, M. *Phys. Rev. C* **86**, 024308 Aug (2012).
126. Gangrsky, Y. P., Marinesky, G. M., Miller, M. B., Samsuk, V. N., and Kharisov, I. F. *Yad. Fiz.* **27**, *894; [Sov. J. Nucl. Phys.* **27** *(1978),475]* (1978).
127. Baas-May, A., Kratz, J. V., and Trautmann, N. *Z. Phys. A* **322**, 457 (1985).
128. Yanbing, X., Shengdong, Z., Huajie, D., Shuanggui, Y., Weifan, Y., Yanning, N., Xiting, L., Yingjun, L., and Yonghou, X. *Phys. Rev. C* **74**, 047303 Oct (2006).
129. Andreyev, A. N., Elseviers, J., Huyse, M., Van Duppen, P., Antalic, S., Barzakh, A., Bree, N., Cocolios, T. E., Comas, V. F., Diriken, J., Fedorov, D., Fedosseev, V., Franchoo, S., Heredia, J. A., Ivanov, O., Köster, U., Marsh, B. A., Nishio, K., Page, R. D., Patronis, N., Seliverstov, M., Tsekhanovich, I., Van den Bergh, P., Van De Walle, J., Venhart, M., Vermote, S., Veselský, M., Wagemans, C., Ichikawa, T., Iwamoto, A., Möller, P., and Sierk, A. J. *Phys. Rev. Lett.* **105**, 252502 Dec (2010).
130. Elseviers, J., Andreyev, A. N., Huyse, M., Van Duppen, P., Antalic, S., Barzakh, A., Bree, N., Cocolios, T. E., Comas, V. F., Diriken, J., Fedorov, D., Fedosseev, V. N., Franchoo, S., Ghys, L., Heredia, J. A., Ivanov, O., Köster, U., Marsh, B. A., Nishio, K., Page, R. D., Patronis, N., Seliverstov, M. D., Tsekhanovich, I., Van den Bergh, P., Van De Walle, J., Venhart, M., Vermote, S., Veselský, M., and Wagemans, C. *Phys. Rev. C* **88**, 044321 Oct (2013).
131. Ghys, L., Andreyev, A. N., Huyse, M., Van Duppen, P., Sels, S., Andel, B., Antalic, S., Barzakh, A., Capponi, L., Cocolios, T. E., Derkx, X., De Witte, H., Elseviers, J.,

Fedorov, D. V., Fedosseev, V. N., Heßberger, F. P., Kalaninová, Z., Köster, U., Lane, J. F. W., Liberati, V., Lynch, K. M., Marsh, B. A., Mitsuoka, S., Möller, P., Nagame, Y., Nishio, K., Ota, S., Pauwels, D., Page, R. D., Popescu, L., Radulov, D., Rajabali, M. M., Randrup, J., Rapisarda, E., Rothe, S., Sandhu, K., Seliverstov, M. D., Sjödin, A. M., Truesdale, V. L., Van Beveren, C., Van den Bergh, P., Wakabayashi, Y., and Warda, M. *Phys. Rev. C* **90**, 041301 Oct (2014).
132. Kuznetsov, V. I. and Skobelev, N. K. *Phys. Part. Nucl.* **30**, 666 (1999).
133. Lazarev, Y. A., Oganessian, Y. T., Shirokovsky, I. V., Tretyakova, S. P., Utyonkov, V. K., and Buklanov, G. V. *EPL (Europhysics Letters)* **4**(8), 893 (1987).
134. Kreek, S. A., Hall, H. L., Gregorich, K. E., Henderson, R. A., Leyba, J. D., Czerwinski, K. R., Kadkhodayan, B., Neu, M. P., Kacher, C. D., Hamilton, T. M., Lane, M. R., Sylwester, E. R., Türler, A., Lee, D. M., Nurmia, M. J., and Hoffman, D. C. *Phys. Rev. C* **49**, 1859–1866 Apr (1994).
135. Hoffman, D. C., Lee, D. M., Gregorich, K. E., Nurmia, M. J., Chadwick, R. B., Chen, K. B., Czerwinski, K. R., Gannett, C. M., Hall, H. L., Henderson, R. A., Kadkhodayan, B., Kreek, S. A., and Leyba, J. D. *Phys. Rev. C* **41**, 631–639 Feb (1990).
136. Shaughnessy, D. A., Adams, J. L., Gregorich, K. E., Lane, M. R., Laue, C. A., Lee, D. M., McGrath, C. A., Patin, J. B., Strellis, D. A., Sylwester, E. R., Wilk, P. A., and Hoffman, D. C. *Phys. Rev. C* **61**, 044609 Mar (2000).
137. Konki, J., Khuyagbaatar, J., Uusitalo, J., Greenlees, P., Auranen, K., Badran, H., Block, M., Briselet, R., Cox, D., Dasgupta, M., Nitto, A. D., Düllmann, C., Grahn, T., Hauschild, K., Herzn, A., Herzberg, R.-D., Heberger, F., Hinde, D., Julin, R., Juutinen, S., Jger, E., Kindler, B., Krier, J., Leino, M., Lommel, B., Lopez-Martens, A., Luong, D., Mallaburn, M., Nishio, K., Pakarinen, J., Papadakis, P., Partanen, J., Peura, P., Rahkila, P., Rezynkina, K., Ruotsalainen, P., Sandzelius, M., Sarn, J., Scholey, C., Sorri, J., Stolze, S., Sulignano, B., Theisen, C., Ward, A., Yakushev, A., and Yakusheva, V. *Physics Letters B* **764**, 265 – 270 (2017).
138. Kaji, D., Morimoto, K., Haba, H., Ideguchi, E., Koura, H., and Morita, K. *Journal of the Physical Society of Japan* **85**(1), 015002 (2016).
139. Wilson, G. L., Takeyama, M., Andreyev, A. N., Andel, B., Antalic, S., Catford, W. N., Ghys, L., Haba, H., Heßberger, F. P., Huang, M., Kaji, D., Kalaninova, Z., Morimoto, K., Morita, K., Murakami, M., Nishio, K., Orlandi, R., Smith, A. G., Tanaka, K., Wakabayashi, Y., and Yamaki, S. *Phys. Rev. C* **96**, 044315 Oct (2017).
140. Fedosseev, V. N., Berg, L. E., Fedorov, D. V., Fink, D., J., L. O., Losito, R., Marsh, B. A., Rossel, R. E., Rothe, S., Seliverstov, M. D., Sjodin, A. M., and Wendt, K. D. A. *Review of Scientific Instruments* **83**(2), 02A903 (2012).
141. Marsh, B. A., Fedosseev, V. N., Fink, D. A., Day Goodacre, T., Rossel, R. E., Rothe, S., Fedorov, D. V., Imai, N., Seliverstov, M. D., and Molkanov, P. *Hyperfine Interactions* **227**(1), 101–111 (2014).
142. Rothe, S., Andreyev, A. N., Antalic, S., Borschevsky, A., Capponi, L., Cocolios, T., De Witte, H., Eliav, E., Fedorov, D., Fedosseev, V., Fink, D., Fritzsche, S., Ghys, L., Huyse, M., Imai, N., Kaldor, U., Kudryavtsev, Y., Koster, U., Lane, J., and Lassen, J. *Nature communications* **4, 1835**, 1 (2013).
143. Ichikawa, T., Iwamoto, A., Möller, P., and Sierk, A. J. *Phys. Rev. C* **86**, 024610 Aug (2012).
144. Möller, P., Randrup, J., and Sierk, A. J. *Phys. Rev. C* **85**, 024306 Feb (2012).
145. Panebianco, S., Sida, J.-L., Goutte, H., Lemaître, J.-F., Dubray, N., and Hilaire, S. *Phys. Rev. C* **86**, 064601 Dec (2012).
146. Andreev, A. V., Adamian, G. G., and Antonenko, N. V. *Phys. Rev. C* **86**, 044315 Oct (2012).
147. Andreev, A. V., Adamian, G. G., Antonenko, N. V., and Andreyev, A. N. *Phys. Rev. C* **88**, 047604 (2013).
148. Andreev, A. V., Adamian, G. G., and Antonenko, N. V. *Phys. Rev. C* **93**, 034620 Mar (2016).
149. Warda, M., Staszczak, A., and Nazarewicz, W. *Phys. Rev. C* **86**, 024601 Aug (2012).
150. McDonnell, J. D., Nazarewicz, W., Sheikh, J. A., Staszczak, A., and Warda, M. *Phys. Rev. C* **90**, 021302 Aug (2014).
151. Möller, P., Madland, D. G., Sierk, A. J., and Iwamoto, A. *Nature* **409**(6822), 785 – 790 (2001).

152. Möller, P. and Randrup, J. *Phys. Rev. C* **91**, 044316 Apr (2015).
153. Randrup, J. and Möller, P. *Phys. Rev. Lett.* **106**, 132503 Mar (2011).
154. Hulet, E. K., Wild, J. F., Dougan, R. J., Lougheed, R. W., Landrum, J. H., Dougan, A. D., Schadel, M., Hahn, R. L., Baisden, P. A., Henderson, C. M., Dupzyk, R. J., Sümmerer, K., and Bethune, G. R. *Phys. Rev. Lett.* **56**, 313–316 Jan (1986).
155. Hulet, E. K., Wild, J. F., Dougan, R. J., Lougheed, R. W., Landrum, J. H., Dougan, A. D., Baisden, P. A., Henderson, C. M., Dupzyk, R. J., Hahn, R. L., Schädel, M., Sümmerer, K., and Bethune, G. R. *Phys. Rev. C* **40**, 770–784 Aug (1989).
156. Martin, J.-F., Taieb, J., Chatillon, A., Bélier, G., Boutoux, G., Ebran, A., Gorbinet, T., Grente, L., Laurent, B., Pellereau, E., Alvarez-Pol, H., Audouin, L., Aumann, T., Ayyad, Y., Benlliure, J., Casarejos, E., Cortina Gil, D., Caamaño, M., Farget, F., Fernández Domínguez, B., Heinz, A., Jurado, B., Kelić-Heil, A., Kurz, N., Nociforo, C., Paradela, C., Pietri, S., Ramos, D., Rodríguez-Sànchez, J.-L., Rodríguez-Tajes, C., Rossi, D., Schmidt, K.-H., Simon, H., Tassan-Got, L., Vargas, J., Voss, B., and Weick, H. *The European Physical Journal A* **51**(12), 1–8 (2015).
157. Itkis, M., Kondrat'ev, N., Mul'gin, S., Okolovich, V., Rusanov, A., and Smirenkin, G. *Sov. J. Nucl. Phys.* **52**, 601 (1990).
158. Itkis, M., Kondrat'ev, N., Mul'gin, S., Okolovich, V., Rusanov, A., and Smirenkin, G. *Sov. J. Nucl. Phys.* **53**, 757 (1991).
159. Nishio, K., Andreyev, A. N., Chapman, R., Derkx, X., Düllmann, C. E., Ghys, L., Heßberger, F., Hirose, K., Ikezoe, H., Khuyagbaatar, J., Kindler, B., Lommel, B., Makii, H., Nishinaka, I., Ohtsuki, T., Pain, S., Sagaidak, R., Tsekhanovich, I., Venhart, M., Wakabayashi, Y., and Yan, S. *Physics Letters B* **748**, 89 – 94 (2015).
160. Prasad, E., Hinde, D. J., Ramachandran, K., Williams, E., Dasgupta, M., Carter, I. P., Cook, K. J., Jeung, D. Y., Luong, D. H., McNeil, S., Palshetkar, C. S., Rafferty, D. C., Simenel, C., Wakhle, A., Khuyagbaatar, J., Düllmann, C. E., Lommel, B., and Kindler, B. *Phys. Rev. C* **91**, 064605 Jun (2015).
161. Tripathi, R., Sodaye, S., Sudarshan, K., Nayak, B. K., Jhingan, A., Pujari, P. K., Mahata, K., Santra, S., Saxena, A., Mirgule, E. T., and Thomas, R. G. *Phys. Rev. C* **92**, 024610 Aug (2015).
162. Shaughnessy, D. A., Gregorich, K. E., Adams, J. L., Lane, M. R., Laue, C. A., Lee, D. M., McGrath, C. A., Ninov, V., Patin, J. B., Strellis, D. A., Sylwester, E. R., Wilk, P. A., and Hoffman, D. C. *Phys. Rev. C* **65**, 024612 (2002).
163. Gangrsky, Y. P., Miller, M. B., Mikhailov, L. V., and Kharisov, I. F. *Yad. Fiz.* **31**, *306; [Sov. J. Nucl. Phys.* **31** *(1980),162]* (1980).
164. Andreyev, A. N., Bogdanov, D. D., Saro, S., Ter-Akopian, G. M., M., V., and Yeremin, A. V. *Phys. Lett. B* **312**(12), 49 – 52 (1993).
165. Mamdouh, A., Pearson, J., Rayet, M., and Tondeur, F. *Nucl. Phys. A* **679**(34), 337 – 358 (2001).
166. Zagrebaev, V., Denikin, A., Alekseev, A. P., Karpov, A. V., Samarin, V. V., Naumenko, M. A., and Kozhin, A. Y.
167. Hall, H. and Hoffman, D. C. *Annual Review of Nuclear and Particle Science* **42**(1), 147–175 (1992).